

Article

Synthesis of Activated Porous Carbon from Red Dragon Fruit Peel Waste for Highly Active Catalytic Reduction in Toxic Organic Dyes

Pitchaimani Veerakumar^{1,2,*} , Shih-Tung Hung¹, Pei-Qi Hung¹ and Veeraraghavan Vishnu Priya²¹ Department of Chemistry, National Taiwan University, Taipei 10617, Taiwan² Department of Biochemistry, Saveetha Dental College and Hospitals, Saveetha Institute of Medical and Technical Sciences, Chennai 600 077, India

* Correspondence: spveerakumar@gmail.com

Abstract: In this study, an alternative precursor for production of biomass-derived activated carbon was introduced using dragon fruit (*Hylocereus costaricensis*) peels. Chemical activators such as FeCl₃, MgCl₂, ZnCl₂ were used in the thermal carbonization process to convert carbon into porous carbon (PC). However, heteroatom-doped PC catalysts including N-, B-, and P-doped carbon catalysts in the field of dye removal is highly desirable. Several approaches (XRD, FE-SEM/TEM, XPS, FT-IR, EDS, and elemental mapping) were employed to examine the surface morphology, surface properties, and elemental composition of the PC catalyst. The catalytic activity of metal-free PC catalyst was demonstrated for methylene blue (MB), crystal violet (CV), and Nile blue (NB) in a mild environment. The corresponding rate constant (k_{app}) values were estimated as 0.2473, 0.3248, and 0.3056 min⁻¹, respectively, for MB, CV, and NB, which were significantly greater than those of numerous reports. It exhibited the best catalytic activity and recyclability. Moreover, the approach proposed here could create new opportunities for the remediation of organic dyes in lakes and industrial wastewater.

Keywords: porous carbon; methylene blue; Nile blue; crystal violet; reduction

Citation: Veerakumar, P.; Hung, S.-T.; Hung, P.-Q.; Vishnu Priya, V. Synthesis of Activated Porous Carbon from Red Dragon Fruit Peel Waste for Highly Active Catalytic Reduction in Toxic Organic Dyes. *Catalysts* **2023**, *13*, 449. <https://doi.org/10.3390/catal13020449>

Academic Editor: Pasquale Fernando Fulvio

Received: 19 January 2023

Revised: 13 February 2023

Accepted: 16 February 2023

Published: 20 February 2023



Copyright: © 2023 by the authors. Licensee MDPI, Basel, Switzerland. This article is an open access article distributed under the terms and conditions of the Creative Commons Attribution (CC BY) license (<https://creativecommons.org/licenses/by/4.0/>).

1. Introduction

In recent years, the development of cost-effective, efficient, and novel catalytic systems is always an important topic for heterogeneous catalysis from academia and industrial points of view [1–7]. Doping different heteroatoms (N, P, B, and S) into the *sp*²-hybridized carbon lattice has been used in catalyst supports [8] and metal-free catalysts [9,10], and thus significantly enhances catalytic efficiency. It can harvest charge delocalization and alter the electronic structure into a metal-like phase, allowing for considerable catalytic performance comparable to metal-based catalysts or serving as a superior alternative to metal catalysts in industrial growths [11]. More importantly, heteroatoms can change their physicochemical and electronic properties, served as catalytic active sites, resulting in an increased ability to catalyze chemical transformations [12]. Based on this strategy, many academics have been working on developing the PC in the fields of organic transformations, energy storage, and sensors [13–20].

Red dragon (*Hylocereus costaricensis*; *H. costaricensis*) is widely grown in southern China, which is consumed freshly or processed in large amounts annually and consumed directly or processed into juice [21]. Dragon fruits have a seed and peel on the outside portion. Most commonly, the outside portion of the peel is thrown away as a biowaste material; it has no commercial value and in fact it often creates a serious problem in solid waste disposal. It has a high moisture content, contains fibers, lignocellulosic compounds, and other minerals [22]. In the present study, conversion of peel waste into porous carbon would increase its economic value, help to reduce the cost of waste disposal, and provide an inexpensive raw material for production of high surface area PCs using different activation processes [23,24].

In chemical activation process, the raw biomass material must be impregnated with some low-cost chemical activators such as KOH, H₃PO₄, FeCl₃, MgCl₂, and ZnCl₂ [25–28]. In addition, doping PCs with heteroatoms has been considered as a possible replacement for metal-based catalysts for organic transformations and dye reduction [29,30]. More specifically, the development of green chemistry and sustainable chemistry has greatly benefited from the use of metal free-carbon-based materials, which has resulted in a variety of novel applications over the past decade [31,32].

Toxic chemicals including dyes, nitro compounds, pesticides, and phenolic compounds can cause contamination of water bodies; however, removal of these pollutants is crucial [33,34]. Particularly, water-soluble organic dyes such as methylene blue (MB) [35], Nile blue (NB) [36], and crystal violet (CV) [37,38] are well-known environmental pollutants that can cause serious environmental and health problems [39]; due to their toxicity, they can also cause hyperactivity and attention deficit hyperactivity disorder (ADHD) in children [40,41]. Wang et al. [42] reported the use of N-doped graphene foam as a metal-free catalyst for the catalytic reduction in MB under mild conditions. Similarly, N-doped porous carbon was made from biowaste (pumpkin) and used as a metal-free catalyst for 2-methyl-4-nitrophenol reduction. The enhancement in catalytic activity was brought about by the presence of N atoms, which change the electronic structure of nearby carbon atoms [43]. Due to the synergistic effect between co-doped heteroatoms, not only do they produce more additional active sites to intensify the catalytic performance for the reduction in dye pollutants, but they also increase electrical conductivity of catalysts to improve electron transfer.

In this article, we describe the N,B,P-doped porous carbon (NBP-PCs), which is an effective metal-free catalyst for the reduction in organic dyes (MB, CV, NB). Several analytical and spectroscopic techniques were used to characterize the catalysts. The NBP-PC synthesized with remarkable reduction ability toward dye pollutants can be attributed to its large specific surface area, easy interaction/diffusion of dye pollutants, rapid transfer of electrons into substrates, and rich content of heteroatoms in the carbon matrix. The heterogamous PC matrix is easy to handle for recycling purposes without decreasing the catalytic efficiency. Thus, the NBP-PCs catalyst delineates a robust, user-friendly, and highly effective system with prospective practical applications for the catalytic reduction in organic dye pollutants.

2. Results and Discussion

2.1. X-ray Diffraction

The X-ray diffractogram spectra of NBP-PC-Mg, NBP-PC-Fe, and NBP-PC-Zn were mentioned in Figure 1a. For all samples, the occurrence of initial broad peak at $2\theta = \sim 10\text{--}12^\circ$ and next at $2\theta = \sim 25\text{--}30^\circ$ while third at $2\theta = \sim 40\text{--}43^\circ$ reveals that all samples had amorphous nature and further reveal the low graphitization degree of the three carbon samples [44]. In addition, it was determined that the characteristic peaks for NBP-PC-Mg ($2\theta = \sim 12.6, 27.9, 42.2^\circ$), NBP-PC-Fe ($2\theta = \sim 11.7^\circ, 30.7^\circ, \text{ and } 42.2^\circ$), and NBP-PC-Zn ($2\theta = \sim 12.2^\circ, 32.2^\circ, \text{ and } 43.1^\circ$) could be attributed to the (002), (100) and (110) planes, respectively. The diffraction peak of NBP-PC-Zn sample became slightly broader at higher intensity compared to the other samples, indicating that the carbon structure was turbostratic in nature [45]. The XRD results confirmed that NBP-PCs has an amorphous-like carbons, and these results were further evaluated by Raman spectroscopic analysis. After the chemical activation process, only $\sim 12, 10, \text{ and } 8$ ppm of Mg, Fe, and Zn species were present, according to an ICP-AES analysis of the prepared carbon catalysts.

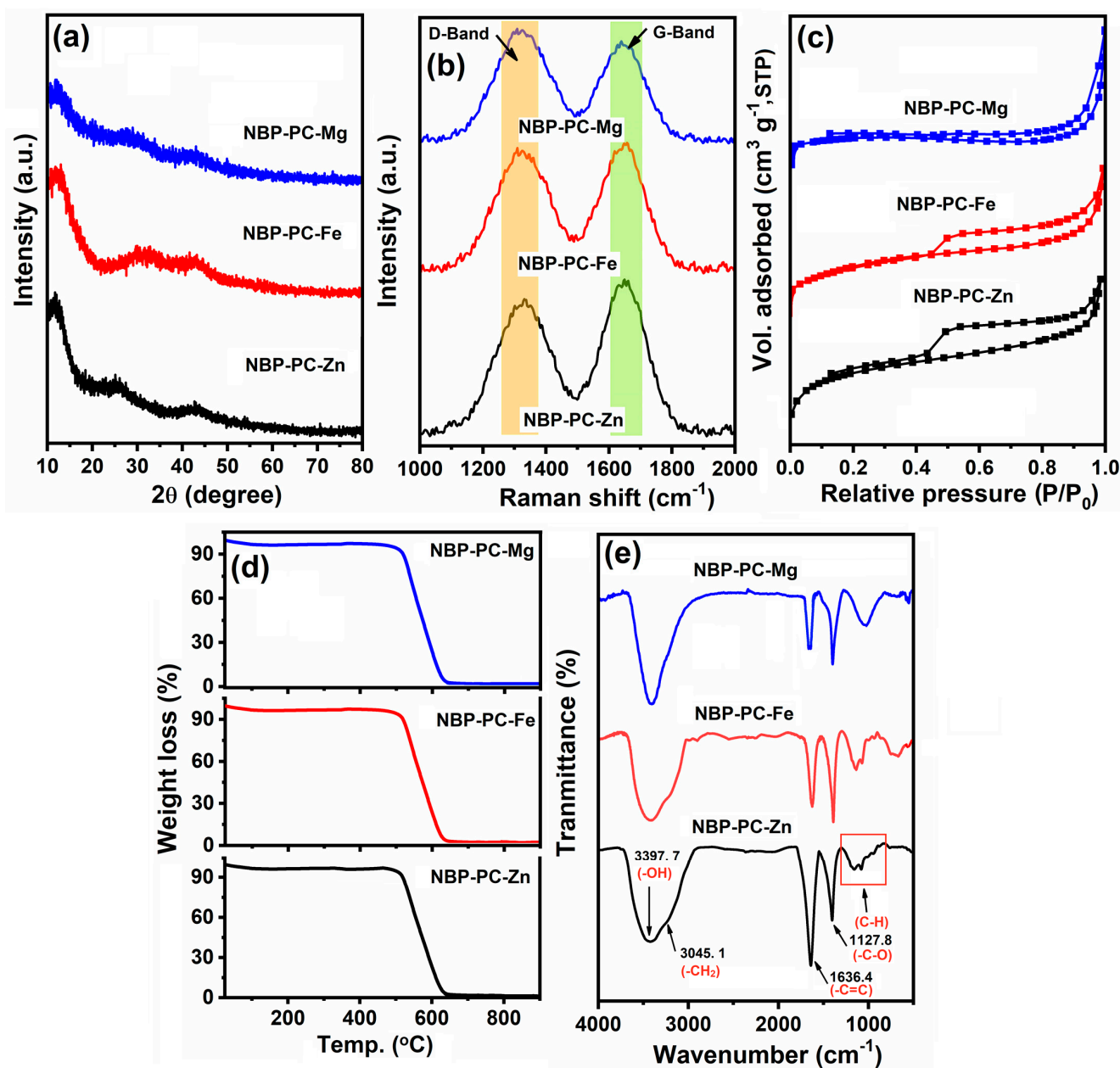


Figure 1. (a) XRD diffractogram, (b) Raman spectra, (c) N_2 -adsorption/desorption isotherms, (d) TGA profiles, and (e) FT-IR spectra of NBP-PC-Mg, NBP-PC-Fe, and NBP-PC-Zn samples.

2.2. Raman Analysis

Raman spectra are further used to reveal the microstructure of as-prepared carbon samples, as shown in Figure 1b. From the analysis, two absorption bands appeared at ~ 1342 and 1608 cm^{-1} , corresponding to the D and G band, respectively. They arise from disordered or defective structure of the sp^3 hybridization (A_{1g} symmetry), whereas the G band represents the E_{2g} phonon vibration of the graphitic sp^2 hybridized carbon atoms, respectively [46]. Therefore, it is possible to evaluate the degree of defects in carbon materials using the intensity ratio of D band to G band (I_D/I_G) values. According to Table 1, all samples had higher I_D/I_G values, indicating that there were more defects after doping of heteroelements into the porous carbon network [47]. These results demonstrate that the graphitization degree was slightly decreased after heteroatoms-doping which introduces defects in the form of N, B, and P functionalities.

Table 1. Physical properties of the as-prepared samples.

| Sample | S_{total} ($\text{m}^2 \text{g}^{-1}$) ^a | S_{micro} ($\text{m}^2 \text{g}^{-1}$) ^b | S_{meso} ($\text{m}^2 \text{g}^{-1}$) ^b | V_{tot} ($\text{cm}^3 \text{g}^{-1}$) ^a | V_{micro} ($\text{cm}^3 \text{g}^{-1}$) ^b | D_P (nm) ^c | I_D/I_G |
|-----------|---|---|--|--|--|-------------------------|-----------|
| NBP-PC-Mg | 851.4 | 368.3 | 483.1 | 0.433 | 0.12 | 2.6 | 0.96 |
| NBP-PC-Fe | 877.5 | 289.2 | 588.3 | 0.454 | 0.13 | 2.3 | 0.94 |
| NBP-PC-Zn | 1000.8 | 487.4 | 513.4 | 0.632 | 0.20 | 5.0 | 1.03 |

^a Total surface areas (S_{tot}) and pore volumes (V_{tot}) derived at $P/P_0 = 0.99$. ^b Microporous surface areas (S_{micro}) and pore volumes (V_{micro}) obtained from t-plot analyses, values in parentheses indicate the portion relative to the total value. ^c Average pore size (D_P) derived by QSDFT method.

2.3. N_2 Isotherms

The textural structure of the obtained porous carbons is investigated by N_2 adsorption at 77 K (Figure 1c). Chemical activation approach yields meso/micropore formation during the pyrolysis at higher temperature. The specific surface area (S_{BET}) was calculated by the following Equation (1) using the N_2 adsorption–desorption isotherm and Brunauer–Emmett–Teller (BET) method [48].

$$\frac{1}{W \left[\left(\frac{P_0}{P} \right) - 1 \right]} = \frac{1}{W_m C} + \frac{C - 1}{W_m C} \left(\frac{P}{P_0} \right), \quad (1)$$

where W is the weight of gas absorbed, P_0/P is the relative pressure, W_m is the weight of adsorbate intended as a monolayer, C is the BET constant expands $\exp(E_1 - E_L/RT)$, E_1 denotes the first layer's heat of adsorption, and E_L means the heat of vaporization. The BET equation describes a linear plot, restricted to $0.05 \leq P/P_0 \leq 0.25$ region of the N_2 adsorption isotherm, of $1/[W(P_0/P) - 1]$ vs. P/P_0 with $C - 1/W_m C$ and $1/W_m C$ as slop and intercept, respectively. The BET surface area is calculated from the slope and the intercept from the following Equation (2):

$$S_{\text{BET}} = \frac{X_m \dot{N} A_{\text{CS}}}{M_v M} \quad (2)$$

where N is the Avogadro's number, A_{CS} is the cross-sectional area of the adsorbate, M_v is the molar volume (22,414 mL), and M is the sample mass. The quantitative analysis of the S_{micro} and $\text{Vol}_{\text{micro}}$ is obtained by means of t-plot method (Carbon Black STSA thickness equation) [49]. The method evaluates the thickness of N_2 as an adsorbate layer as a function of P/P_0 with $0.05 \leq P/P_0 \leq 0.42$ compared to non-porous material. From the linear curve extrapolated to the P/P_0 axis, V_{micro} and S_{micro} are determined as the intercept and slope, respectively. The layer thickness equation is based on the carbon standard (carbon black STSA, Equation (3)).

$$\text{Carbon Black STSA thickness equation } (t) = 0.88 (P/P_0)^2 + 6.45 (P/P_0) + 2.98. \quad (3)$$

As a result, all the samples exhibit mixture of type-I and type-II isotherms, the sharp adsorption at a lower relative pressure revealing the presence of micropores, whereas the hysteresis loop at a higher relative pressure (0.42) implies the existence of mesopores (see Figure 1c) according to the International Union of Pure and Applied Chemistry (IUPAC) [50].

Besides that, pore size distribution (PSD) was calculated using Quenched Solid Density Functional Theory (QSDFT) equilibrium model. Figure S1a confirms the existence of micro/mesopores. The textural properties of these samples are summarized in Table 1 in detail. Surface area and pore size distribution of the all samples were characterized using analysis of N_2 sorption isotherms (Figure 1c). The isotherm shape corresponds to exhibit mixture of type-I and type-II isotherms, which is typically assigned to slit pores (Figure S1b). The BET surface of the NBP-PC-Zn sample is $1000.8 \text{ m}^2 \text{g}^{-1}$, which is significantly higher than the BET surfaces of the NBP-PC-Fe and NBP-PC-Mg samples. However, compared to NBP-PC-Zn sample, NBP-PC-Mg produced less specific surface area ($851.4 \text{ m}^2 \text{g}^{-1}$).

According to these findings, activation with Mg slightly decreased the carbon's specific surface area while activation with Zn significantly increased it. Since NBP-PC-Zn had a higher value than other samples and the corresponding pore volume of NBP-PC-Mg, NBP-PC-Fe, and NBP-PC-Zn was 0.433, 0.454 and 0.632 cm³ g⁻¹, respectively (Table 1), the high surface area and narrower pore size distribution may benefit electron transport by providing high absorbance dye or toxic substance transport channels to micropores [51].

2.4. Thermogravimetric Analysis

The TGA profiles were used to assess the variation in the thermal characteristics of the produced carbon samples (Figure 1d) and differential thermal analysis (DTA, Figure S1c). The first weight loss (approximately ~2.8%) at 100 °C could be elimination of absorbed water. The combustion of carbon (carboxyl and carbonyl groups) detected on the surface of the PCs caused additional single step mass loss at 350 °C [52]. The decomposition of cellulosic and lignocellulosic fragments is most likely the cause of the temperature range between 400 and 660 °C at which carbon burns off from all activated samples. Following the completion of the acid washing process, all the carbons typically have residual masses of less than 0.5 weight percent, indicating that they are essentially entirely carbonaceous and contain only minute amounts of mineral matter [53].

2.5. FT-IR Analysis

As shown in Figure S2, the FT-IR spectra of raw dragon fruit peel and carbon samples were recorded. It could be clearly seen that the dry dragon fruit shows four strong absorption peaks at ~3500~1000 cm⁻¹. These peaks could be attributed to the characteristic peaks of the antisymmetric stretching mode of -OH (~3397.7 cm⁻¹), -CH₃ and -CH₂ (~3045.1 cm⁻¹), respectively [54]. The peak at ~1127.8 cm⁻¹ was attributed to the vibration mode of C-O, suggesting that it may relate to cellulose and hemicelluloses moiety [55]. In addition, the peak at ~1636.4 cm⁻¹ correlates to the C=C skeletal vibration frequency of graphene sheet [56]. The typical transmittance peaks of the functional groups -OH, C=O, and C-O still appeared in all samples and the peak positions were nearly the same, suggesting that the carbon framework and functional groups were analogous to each other (see Figure 1e). Importantly, the main graphene peaks are also noticeable without shifts in the FTIR spectra of as-prepared PCs. As a result, graphene-like nanostructures may be made in lignin-based carbons using our protocols [57].

2.6. Structural Properties

The morphology of the samples was further carried out using FE-TEM and STEM-EDS mapping. Figure 2a–c shows the crumpled ultrathin nanosheets-like morphology of NBP-PC-Mg sample along with tiny voids within nanosheets. Notably, the interconnected pore channels are primarily necessary for organic pollutants, fast dye diffusion, and adsorption. As can be seen in Figure 2d–f, the FE-TEM images of NBP-PC-Fe sample show porous multilayer texture with mesoporous. The images of TEM (Figure 2f) prove the successful preparation of NBP-PC-Fe. It exhibited porous morphology with disorderly, unsystematic pores spread on the surface, and some pore channels in the carbon domains are distinguishable, which could be attributed to generation of different iron compounds derived from FeCl₃ [58]. Furthermore, abundant holes were observed on the edges and wrinkles across the entire sheets. TEM analysis is employed to further explore the microstructure of NBP-PC-Zn material in Figure 2g–i. The images show the formation of irregular and discontinuous cracks were observable on NBP-PC-Zn surface. This is due to the effect of ZnCl₂ evaporation during the pyrolysis process and the potential development of pores that ZnCl₂ may have previously occupied but was washed out during the HCl-rinsing steps. In addition, the localized graphitic structure can be seen from high-resolution FE-TEM image in Figure 2i, which reveal graphitic layers in the carbon matrix. The small graphitic layers show considerable defects and edges on the surface of the Zn activated carbon.

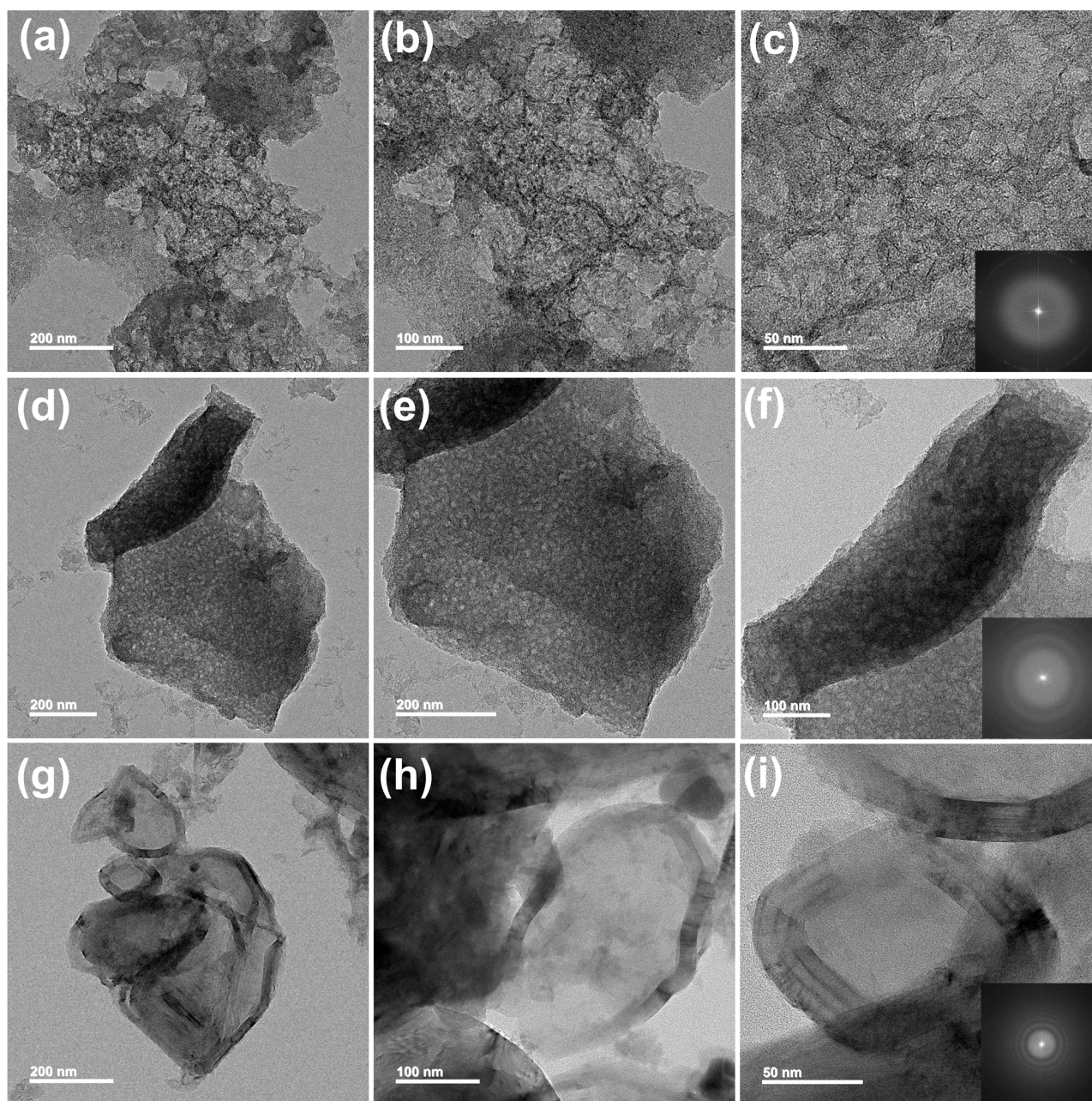


Figure 2. FE-TEM images of the (a–c) NBP-PC-Mg, (d–f) NBP-PC-Fe, and (g–i) NBP-PC-Zn samples (Inset: c, f and i are show the related FFT patterns).

Furthermore, typical fast Fourier transform (FFT, inset: Figure 2b,d,f) reveals the carbon samples are of an amorphous nature. FE-TEM-EDS line-scan analysis was applied along a linear path passing through the peripheral and central parts of a representative elements present in the NBP-PC-Zn sample (see Figure S3).

Furthermore, typical high-angle annular-dark field scanning transmission electron microscopic (HAADF-STEM) image and corresponding EDS mapping images are shown in Figure 3a–f. From the images, it can be observed that a homogeneous distribution of N, B, P, C, and O elements was present in the skeleton of NBP-PC-Zn sample, and resultant EDS spectrum is shown in Figure 3g. In addition, the HAADF-STEM images (Figures S4 and S5) and elemental mapping analysis were carried out to confirm the existence of C, O, N, B, and P elements are distributed in NBP-PC-Mg and NBP-PC-Fe samples.

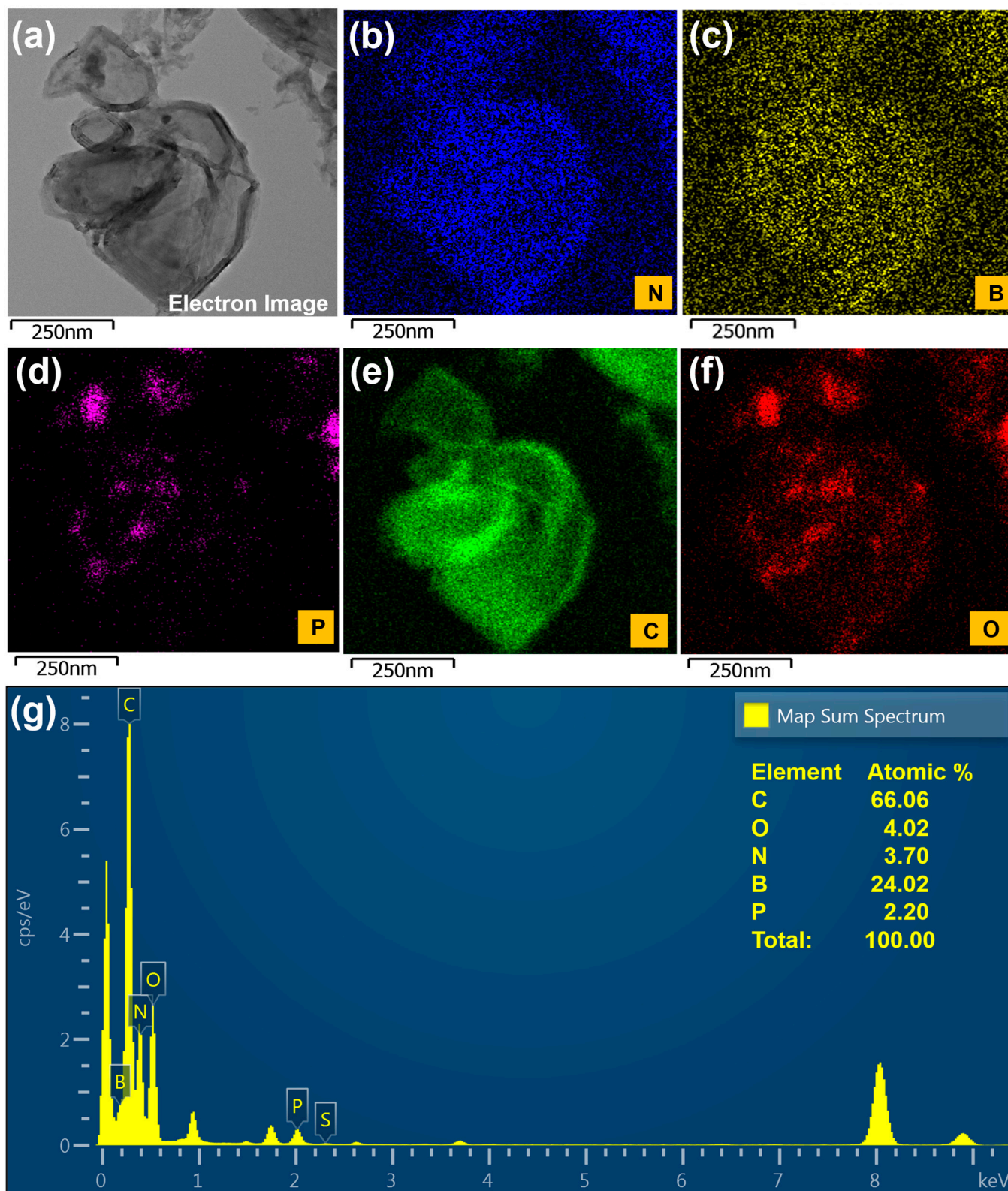


Figure 3. (a) STEM image, (b–f) element mapping (N, B, P, C, and O elements), and (g) EDS results of NBP-PC-Zn sample.

The PCs were subsequently investigated by XPS analysis. The XPS data suggest that the material contains C (90.24 at%), O (5.01 at%), B (2.03 at%), N (1.57 at%), and a small quantity of P (1.15 at%), as shown in XPS survey spectrum Figure 4a. As observed

from the N 1s (Figure 4b), spectra were partitioned into four peaks for NBP-PC-Zn assigned, namely pyridinic-N (398.2 ± 0.02 eV), pyrrolic-N (399.7 ± 0.02 eV), quaternary-N (401.1 ± 0.01 eV), and N-oxide (402.9 ± 0.03 eV), respectively [59], whereas the N present in the NBP-PC-Fe sample could be sorted into three species (Figure 4b): pyridinic-N (398.4 ± 0.02 eV), pyrrolic-N (399.9 ± 0.01 eV), and quaternary-N (401.7 ± 0.02 eV). However, the core-level N 1s XPS spectrum of NBP-PC-Mg sample shows photoelectron signal BE at 398.5 ± 0.02 eV and 400.1 ± 0.01 eV for pyridinic-N and pyrrolic-N species, respectively. Of particular interest are graphitic-N and pyridinic-N, able to enhance the catalytic activity because of their N species; they use four electrons to generate bonds of σ and π , as well as the remaining electron to occupy the higher-energy π^* state, resulting in the electron donor property of N contributing to metal-free catalyst [60].

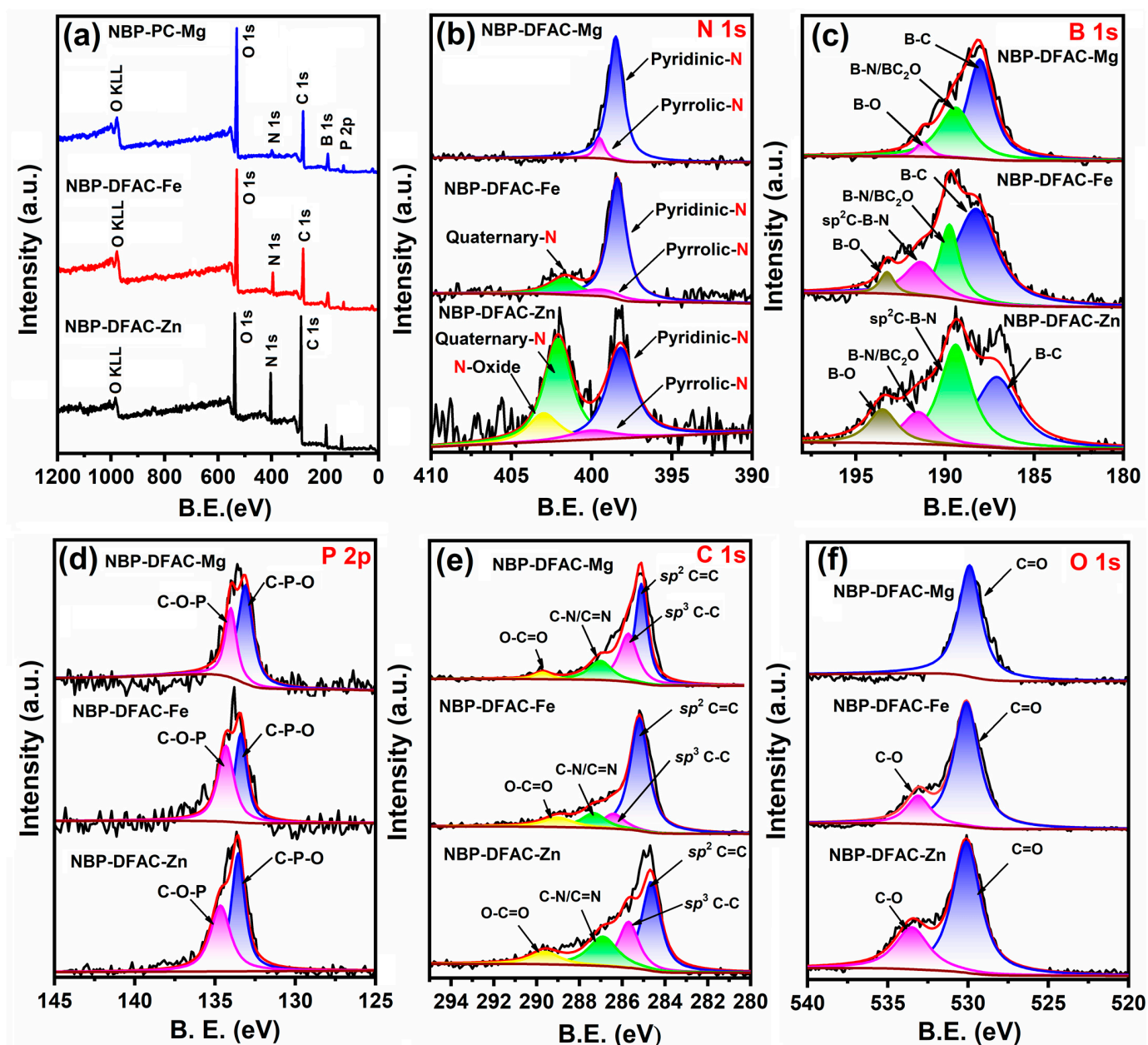


Figure 4. (a) XPS survey spectrum and (b–f) high resolution XPS spectra of N 1s, B 1s, P 2p, C 1s, and O 1s.

The high-resolution B 1 s spectrum of NBP-PC-Mg (Figure 4c) shows three peaks at $\sim 190.9 \pm 0.02$, 191.8 ± 0.01 , and 193.0 ± 0.02 eV corresponding to boron species (B–C, BN/BC₂O, and B–O) [61]. The NBP-PC-Fe sample can be divided into four major peaks at $\sim 187.1 \pm 0.01$, 189.4 ± 0.02 , 191.5 ± 0.02 , 193.5 ± 0.02 eV which are related to B–C, BN/BC₂O, *sp*²C–B–N, and B–O bonds. Nonetheless, the B 1 s spectrum of NBP-PC-Zn is performed; there are obvious four peaks centered at ($\sim 187.1 \pm 0.01$ eV, B–C), (189.0 ± 0.03 eV, BN/BC₂O), (191.2 ± 0.02 eV, *sp*²C–B–N), and (193.1 ± 0.01 eV, B–O). As a result, these data clearly demonstrate the successful B-doping in all carbon samples.

The P 2 p spectrum (Figure 4d) of NBP-PC-Zn sample clearly displayed the presence of two strong peaks at $\sim 133.3 \pm 0.02$ and 134.8 ± 0.01 eV, corresponding to C–P–O (the P atom doped into the carbon lattice) and C–O–P (the formation of an oxygen bridge between C and P) bonds [62]. Similarly, NBP-PC-Fe sample displays two peaks that appeared at the B.E of 133.6 ± 0.03 and 134.5 ± 0.02 eV were C–P–O and C–O–P, respectively. The oxygen atoms in the P–O bond would increase the electron depletion of the carbon atoms, causing electron delocalization, and the doped P would induce negatively delocalized C atoms adjacent to the P atoms, according to the literature reports [63,64]. As a result, P doping has the ability to create defect sites and significantly change the chemical reactivity and electronic characteristics of PC materials. The performance of catalysts was improved as a result of these surface modifications [65].

From Figure 4e, it can be observed that the core XPS spectrum of C 1s displays four intense peaks: (i) 284.9 ± 0.02 eV (*sp*² C=C), (ii) 285.2 ± 0.03 eV (*sp*³ C–C), indicating the existence of graphitic carbon, (iii) 286.8 ± 0.01 eV, which is due to the presence of C–N/C=N bonds, and (iv) 289.1 ± 0.01 eV, arising from the O–C=O bonds [66]. Likewise, the same peaks can be observed for NBP-PC-Fe and NBP-PC-Mg samples (see Figure 4e and Table S2). We determine that the O 1s spectrum (Figure 4f) can be fitted with two peaks that represent 531.6 ± 0.01 eV (C=O) and 533.0 ± 0.02 eV (C–O) for NBP-PC-Zn sample [67], while the O 1s spectrum for NBP-PC-Mg sample shows peak with B.E at 529.9 ± 0.01 eV, implying the presence of different O-containing functional groups. It is worth noting that the O 1s peak split into two peaks in the samples NBP-PC-Fe and NBP-PC-Zn rather than the sample NBP-PC-Mg indicates an increase in O content during chemical activation treatment. Table S2 shows a summary of XPS data of N 1 s, B 1 s, P 2 p, C 1 s, and O 1 s elements obtained from fitting calculations, BE values, and their respective assignments.

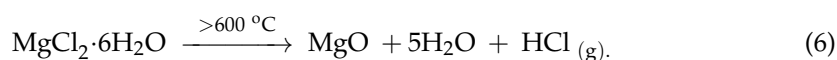
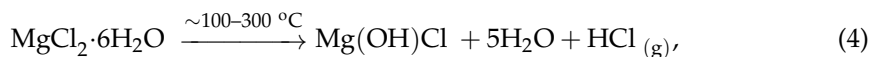
2.7. Role of Chemical Activation

Chemical activation is now more commonly used to produce biomass-derived PCs due to lower activation temperatures (400–700 °C), shorter activation times, higher yield, higher SSA, and well-developed pores. Chemical compounds such as acid, alkali, or metal salts are used in the chemical treatment at lower temperatures [68]. In general, chemical activation is preferable to physical activation because it produces more PCs with superior surface chemistry and textural qualities at a lower activation temperature. The mode of activation and working temperatures, on the other hand, are dependent on the chemical agent used.

2.8. MgCl₂ Activation

It is a nontoxic, noncorrosive, and low-cost activator that has been used to make PCs for adsorption, catalysis, and energy storage [69]. Initially, a partial decomposition of MgCl₂ into Mg(OH)Cl occurs at 100–300 °C due to dehydration reaction, as in Equation (3). When the temperature is raised from 300 to 500 °C, the transformation of Mg(OH)Cl into MgO species is shown in Equation (4) [70]. In contrast, once the temperature reaches >600 °C, the partially hydrated MgCl₂ in Equation (5) decomposes directly into MgO [71]. Carbonized PC gradually covered MgO grains at this stage, inhibiting MgO aggregation. The salt form of MgCl₂ is formed after washing the MgO grains with an acid solution. At this stage, MgO grains were gradually covered by carbonized PC, which also prevented MgO from aggregating. The MgO grains become MgCl₂ after being washed in an acidic

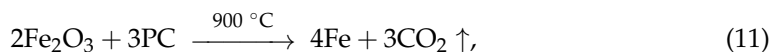
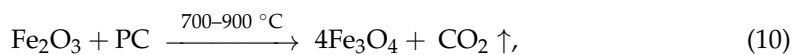
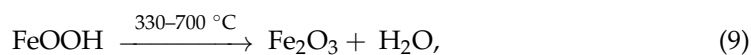
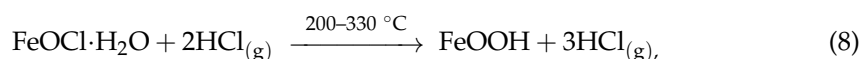
solution. The development of micro/mesopore structures on the surface of PCs is the final development. Equations (4)–(6) can be used to show the potential carbonization pathway for the MgCl_2 in the mixture.



However, the use of MgCl_2 to prepare biomass carbon has only been mentioned a few times in the literature. As a result, the goal of this research is to investigate the use of MgCl_2 in the highly efficient and environmentally friendly manufacture of PC for use as a metal-free catalyst.

2.9. FeCl_3 Activation

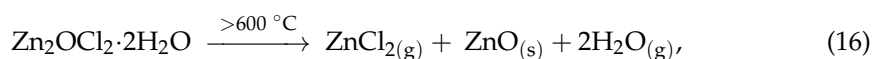
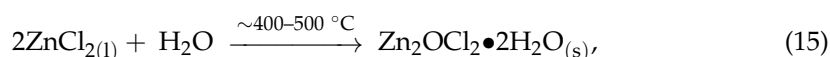
It is the most commonly used reagent for activating biomass-derived carbons [72]. The activation of FeCl_3 produces a rough carbon surface with a high SSA and a porous structure, which is useful in sustainable applications [73]. Commonly, FeCl_3 activation mechanism for activating biomass-derived carbons is possibly based on the following chemical reactions. Initially, FeCl_3 dissociates in water into Fe^{3+} and Cl^- ions, and adsorption between Fe^{3+} ions and PC occurs at RT. As given in Equation (7), $\text{Fe}^{(\text{III})}$ ions react with water molecules to form hydrated iron chloride salt ($\text{FeOCl} \cdot \text{H}_2\text{O}$) and which is further decomposed into amorphous Fe-species (e.g., FeOOH) during this temperature range 200–300 °C. The amorphous FeOOH species transformations are explained by Equation (8) [74]. The second stage occurs at carbonization temperatures between 330–700 °C. During this stage, FeOOH first decompose into Fe_2O_3 , which is subsequently reduced by the PCs surface to form Fe_3O_4 according to the following Equations (9) and (10) [75]. At elevated temperature (~700–900 °C), these iron oxides (Fe_2O_3 and Fe_3O_4) react with carbon matrix, which are completely reduced to zero-valent Fe^0 and deposited on the carbon surface (see Equations (11)–(13)). After the removal of the Fe^0 species in the acid washing step and generation of the meso/micropores on the carbon matrix, further change in the PCs structure occurred.



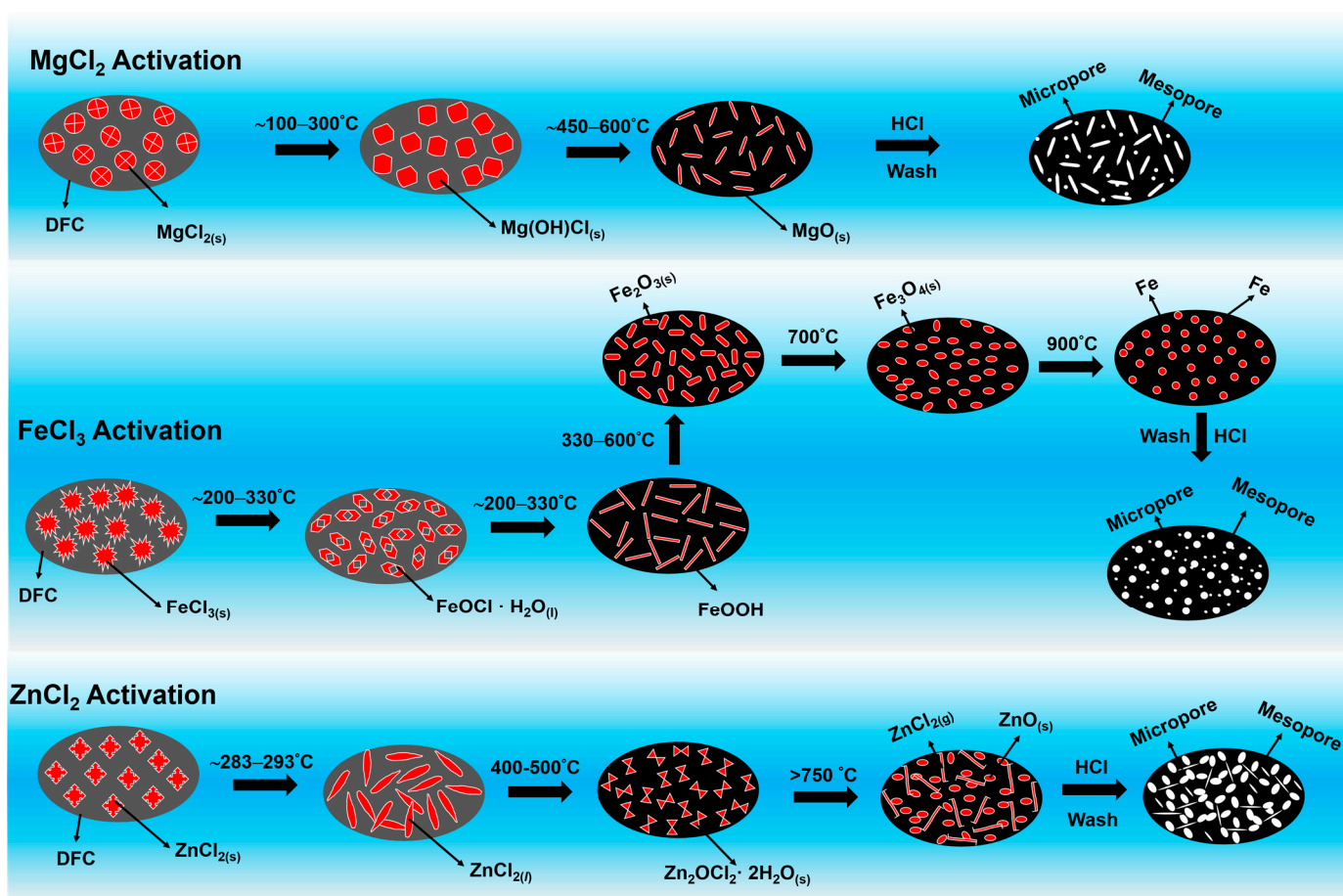
2.10. ZnCl_2 Activation

It is yet another chemical activation agent that is frequently used to transform carbons derived from biomass into PCs [76]. Although this technique is frequently used to make PCs, its exact mechanism is unknown. Additionally, it dehydrates the body during the activation process and deoxygenates the air at high temperatures by removing oxygen in the form of water and reducing the carbohydrate content. Zn^{2+} has a radius of 74 pm, which is less than that of common metal salt ions such as Na^+ (102 pm), K^+ (138 pm), and Ca^{2+} (100 pm),

which may aid in the PC's ability to create large micropores [77]. The impregnated ZnCl₂ tends to transform mobile liquid ZnCl₂ during the process, therefore it should be generated during the first stage of activation at a low melting point of ~283–293 °C (see Equation (13)). The mobile liquid should be able to diffuse, allowing for better contact with the PC surface. Zinc oxide chloride hydrate (ZnOCl₂•2H₂O) may then be formed as a result of a reaction between the fused Zn species and water molecules (see Equation (15)). At the activation temperature of 400–500 °C, the complex (i.e. zinc oxide chloride hydrate) can successively decompose into the gaseous form of ZnCl₂. Significant collapses of the carbon interlayers and the development of matrix pores occur when the activation temperature is elevated above 750 °C (the boiling point of ZnCl₂) due to intensive interactions between carbon atoms and Zn species [78]. Additionally, routes through the PC surface would develop for the diffusion of ZnCl₂ gas and the production of minute ZnO species, causing the more porous structure of the final carbon product, according to the reactions in Equation (16). Once ZnO species were eliminated by an acid wash and drying process, the remaining cavities provided more porosity in the interior structure, as illustrated in Equation (17).



There are various benefits to ZnCl₂ activation: (i) At temperatures above the chemical agent's melting point, liquid ZnCl₂ is intercalated into the PC matrix to produce pores; (ii) in the extended interlayers of carbon, the reaction between the carbon atoms and dehydrating agent is promoted and this activation creates the pathways of pores and restricts the formation of tar, and (iii) it increases the carbon content through the formation of aromatic graphitic structure. (iv) The process speeds up the aromatization process while promoting the dehydrogenation and dehydrocyclization of alkanes and alkenes. It may also create Lewis acid sites associated with Zn species (Zn-L). (v) Another significant source of aromatics was the Diels–Alder reaction (cyclization), which Zn-L was capable of catalyzing. (vi) As a result, a lot of acid sites (primarily Lewis acid sites) whose catalytic effect increased the aromatic content and produced surface functionalities in the activation reaction formed on the carbon catalyst surface, and (vii) some strong acid sites were effective in promoting the hydrogen transfer reaction [79]. However, excessive ZnCl₂ addition may significantly damage the micropore structure while enhancing the mesoporous development, which reduces the surface area. Moreover, a schematic figure in Scheme 1 illustrated the activation procedures of MgCl₂, FeCl₃, and ZnCl₂. The aforementioned findings suggest that ZnCl₂ activation is superior to other types at the same thermal conditions, which can result in appreciable variations in the final activated carbons' pore properties.



Scheme 1. Schematic illustration for the chemical activation process.

2.11. Role of N-, B-, and P-Doping

Heteroatoms, (N, B, and P)-doped porous carbon materials, have generated new structures and different morphologies that are being extensively researched as metal-free catalysts in recent years. The N-doped porous carbon atom has likely received the most attention among other heteroatoms in respect to creation of heteroatom-doped carbons (as a dopant for C) due to the following factors [80]: (i) N can be incorporated into the PC matrix in different locations, leading to a variety of possible configurations; (ii) N can incorporate into the PC matrix at various locations, making it lead to multiple possible configurations; (iii) N-doped carbon materials have a low risk of health issues and are readily available and abundant; (iv) experimental and theoretical research has shown that graphitic, pyridinic, and pyrrolic of N core species interact with pollutants effectively, for example, with dyes or poisonous substances [81]. The presence of N atoms often confers a basic characteristic, which enhances the interaction between acidic molecules and the carbon surface [82]. More crucially, because C (2.55) and N (3.04) have differing electronegativity values, N-doping can significantly affect the charge distribution and spin density of carbon atoms, resulting in the creation of defects in the carbon framework. This in turn may change the carbon framework's electrical structure [83].

Similar to B, which is carbon's left-hand neighbour in the periodic table and has essentially distinct and incomparable properties, B is a good choice for inclusion into carbon sheets [84]. The B-doping in the graphitic framework affects the (optical) electrical and electronic characteristics resulting from the high electron-withdrawing capacity of B (electronegativity: 2.04), which does not only increase the thermal stability of the carbon structures [85].

Next, P is a member of the fifth group element in the periodic table, has nearly identical chemical and electrical properties to those of N and has the same amount of valence electrons [86]. However, compared to carbon atoms (which have a radius of 2.55), it has a larger atomic radius, a lower electronegativity (2.19), and a longer covalent radius. The texture and electrical structure of the carbon layer have been modified by doping with P atoms in either the interstitial or substitutional regions of the lattice to form P-N or P-C bonds. Additionally, the two lone pairs of electrons that P atoms have in their sp^3 orbitals allow charge to advance on the electrode surface and exacerbate flaws in PC nanosheets [87]. Indeed, compared to undoped carbon, P-doped PC exhibits an increase in electric conductivity that is up to four orders of magnitude greater, indicating a higher charge carrier density that facilitates transport in solar and electrochemical applications [88]. This is because P-doped carbon has been modified to boost their active surface sites, which in turn expands the electrical possibilities and reflects the potential applications. P-doping can thereby effectively change the chemical reactivity and electrical characteristics of carbon materials by creating defect sites (pristine carbons). The performance of catalysts is enhanced as a result of these surface changes.

2.12. Reduction in Organic Dyes

As previously indicated, heteroatom-doped PC is significantly more affordable than transition or precious metals, which have been widely used as metal-free catalysts [89]. Environmentally harmful organic dyes such as MB, NB, and CV have been utilized extensively in manufacturing industries [90]. Therefore, this work's challenge is to establish an effective and dependable method for catalyzing the reduction in organic dyes.

Sodium borohydride (NaBH_4) is a white-to-grey crystalline powder that slowly reacts with polar protic solvents (moderate reagent). It has a significant position due to its high hydrogen density, adjustable H_2 generation rate, non-flammability, outstanding stability in alkaline solution, and nontoxic hydrolysis byproducts [91]. On a production scale, it is a reagent that is readily accessible on the market and is increasingly employed for the selective reduction in organic compounds and dyes. In addition, it is employed as a reducing agent in the manufacturing of many pharmaceutical compounds in industries since it is less expensive. A number of factors mitigate in choosing this reagent over other, more traditional reducing agents. However, it can irritate the lungs, causing coughing and/or shortness of breath. Higher exposures can cause a build-up of fluid in the lungs (pulmonary edema), a medical emergency with severe shortness of breath [92].

Water-soluble cationic dye MB is most frequently detected in an ionic form (MB^+) in an aqueous solution. The not-observed adverse effect level (NOAEL) of MB was ca. 25 mg kg^{-1} . The oxidized form of MB generally displays absorption maxima at $\lambda_{\text{max}} = 665 \text{ nm}$, which can be attributed to the $n \rightarrow \pi^*$ transitions, and UV-vis absorption peak in the wavelength (λ) range of 550–750 nm. As a result, UV-vis absorption spectrophotometry makes it simple to monitor the reaction's development. In this experiment, it was shown that the absorbance value at $\lambda_{\text{max}} = 665, 614, \text{ and } 292 \text{ nm}$ gradually declined. As shown in Figure 5a, this reduction reaction typically took place in the presence of 0.6 mg of NBP-PC-Zn (i.e., a metal-free catalyst) in 12 min at RT. The transformation of MB from an intense blue colour to a colourless leuco-methylene blue may indicate a complete reduction in MB by NaBH_4 (LMB).

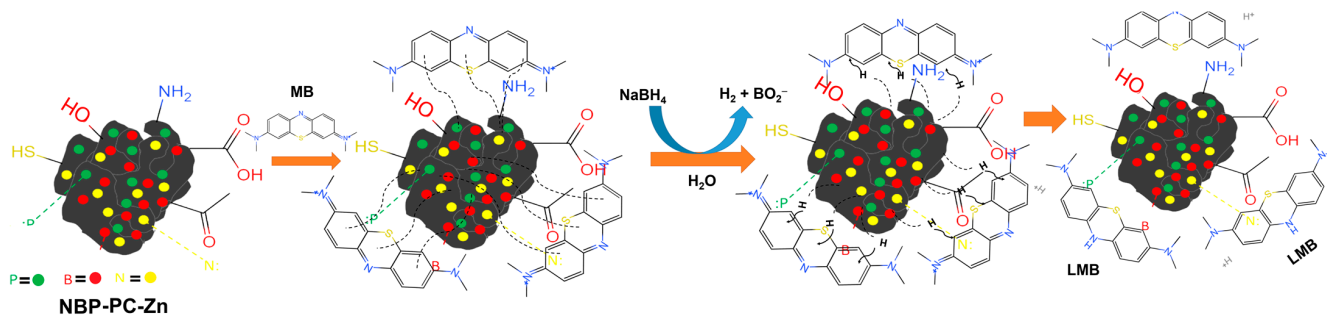


Figure 5. Possible catalytic mechanism of MB reduction over NBP-PC-Zn using NaBH₄.

Crystal Violet (CV) enters into the aquatic systems from the effluents of textile industry, paint industry and also from medical and biotechnology industry. It is well known for its mutagenic, teratogenic and mitotic poisoning nature. The existence of CV dye in a water body, even in just 1 ppm in concentration, causes periodic changes in the intensity of UV absorption maxima at $\lambda_{\max} = 580$ nm, which was noticed at various time intervals (min). The absorption intensity of CV at $\lambda_{\max} = 580$ nm gradually reduced during 10.5 min after catalyst addition, but the intensity at $\lambda_{\max} = 260$ nm increased (Figure 6b). Leuco crystal violet (LCV, colourless) products were produced during the reaction, which caused an abrupt shift in the colour of the solution from violet to colourless and the k_{app} value ca. 3248 min^{-1} . The UV-vis absorption peak at $\lambda_{\max} = 612$ nm also consistently decreased over the course of 12.4 min, demonstrating a successful conversion of NB to leuco-Nile blue (LNB; Figure 6c) [93]. For this dye, the value of k_{app} was estimated to be 0.3056 min^{-1} at room temperature. The obtained results of k_{app} values over other catalysts for this reaction were compared and presented in Figure 6d. Among them, the highest catalytic rate was estimated to be 0.146, 0.1614, and 0.2473 min^{-1} for MB by NBP-PC-Mg, NBP-PC-Fe, and NBP-PC-Zn, respectively. Additionally, Figure 6e depicts the matching colour changes that occurred after the reduction in MB, CV, and NB dyes.

Reduction in MB was selected as a model reaction here in order to assess metal-free reduction catalyst and to improve the reaction conditions. The catalytic performances during the reduction in MB over several types of metal-free catalysts were also examined for comparison. A null reduction was typically produced from reactions when there was no NaBH₄ (hydrogen donor) supplied (entry 1, Figure S6). This was also true for reactions when there was no catalyst present. According to Table 2, bare DFC (entry 2, without chemical activation) showed very little ability to reduce MB dye, but chemically activated catalyst (PC-Zn, entry 3) likewise produced very little reduction, typically between 10 and 25%. As a result, chemical-activated DFC are inexpensive as metal-free catalysts for MB reduction, which is caused by the substrate increased surface areas and active functionalities [81,89]. In contrast, the same reaction was conducted over N-PC-Zn, B-PC-Zn, and P-PC-Zn catalysts under the identical reaction conditions, and it was discovered to proceed quite quickly. All of these catalysts produced reasonable k values for MB reduction (see entries 4–9). The effectiveness of various NBP-PC-Mg (entry 10) and NBP-PC-Fe (entry 11) and catalysts during the reduction in MB was evaluated. Additionally, it is possible to deduce that the catalyst amount increases the k value (entry 12,13). Comparing NBP-PC-Fe (entry 14) to other metal-free catalysts, an outstanding k value was determined, as shown in Table 2.

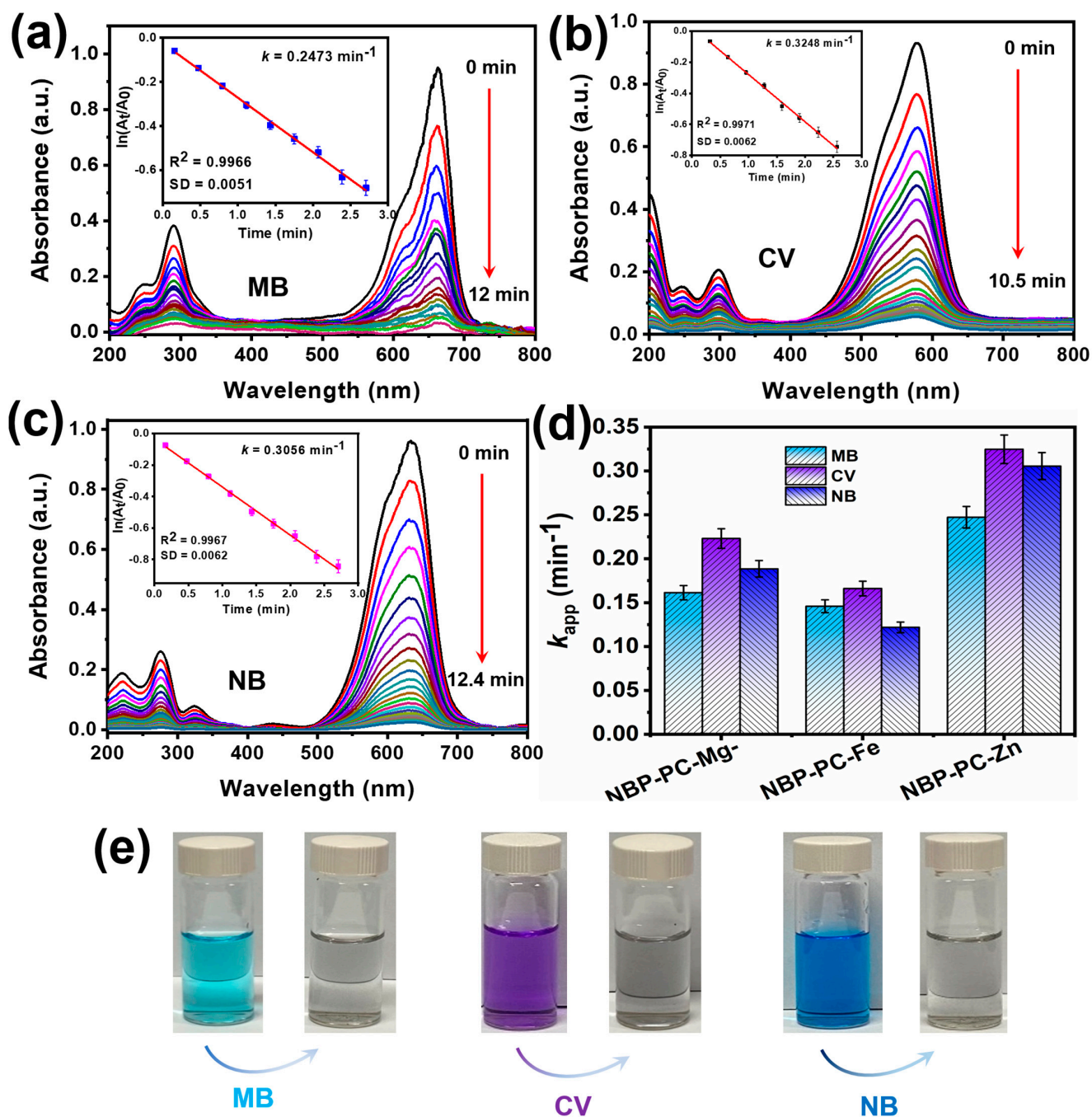


Figure 6. UV-visible absorption spectra of (a) MB, (b) NB, (c) CV after the addition of NaBH₄ in the presence of NBP-PC-Zn (0.6 mg) catalyst, (d) the photographs of colour changes after the dye reductions. (e) the matching colour changes that occurred after the reduction in MB, CV, and NB dyes.

Table 2. Comparison of the MB dye reduction performances of as-prepared carbon catalysts ^a.

| Entry | Catalyst | Catalyst (mg) | Time (min) | k_{app} (min^{-1}) | K ($\text{min}^{-1} \text{mg}^{-1}$) ^b | TOF (min^{-1}) ^c |
|-------|-----------|---------------|------------|---------------------------------|---|--|
| 1 | – | 1.0 | 30 | – | – | – |
| 2 | DFC | 2.0 | 30 | 0.0103 | 0.0103 | 3.3×10^{-4} |
| 3 | PC-Zn | 1.0 | 30 | 0.0255 | 0.0255 | 6.6×10^{-4} |
| 4 | N-PC-Zn | 1.0 | 30 | 0.0483 | 0.0483 | 6.6×10^{-4} |
| 5 | B-PC-Zn | 1.0 | 30 | 0.0462 | 0.0462 | 6.6×10^{-4} |
| 6 | P-PC-Zn | 1.0 | 30 | 0.0397 | 0.0397 | 6.6×10^{-4} |
| 7 | NB-PC-Zn | 1.0 | 30 | 0.0565 | 0.0565 | 6.6×10^{-4} |
| 8 | BP-PC-Zn | 1.0 | 30 | 0.0544 | 0.0544 | 6.6×10^{-4} |
| 9 | NP-PC-Zn | 1.0 | 30 | 0.0498 | 0.0498 | 6.6×10^{-4} |
| 10 | NBP-PC-Mg | 1.0 | 22.2 | 0.1614 | 0.1614 | 9.0×10^{-4} |
| 11 | NBP-PC-Fe | 1.0 | 25.5 | 0.1460 | 0.1460 | 7.9×10^{-4} |
| 12 | NBP-PC-Zn | 0.2 | 12.0 | 0.0685 | 0.3425 | 8.3×10^{-3} |
| 13 | NBP-PC-Zn | 0.4 | 12.0 | 0.1398 | 0.3495 | 4.1×10^{-3} |
| 14 | NBP-PC-Zn | 0.6 | 12.0 | 0.2473 | 0.4122 | 2.7×10^{-4} |

^a Reaction conditions: catalyst (1.0 mg), MB (20 mL of 0.1 mM), NaBH_4 (0.25 M) at 25 °C. ^b $K = \frac{k_{app}}{\text{the amount of catalyst}}$.

^c $\text{TOF} = \frac{\text{mM of MB}}{\text{mg catalyst per min}}$.

Only NaBH_4 was added to the MB solution, and after 20 min, there was almost no drop in the absorption intensity at $\lambda_{\text{max}} = 665 \text{ nm}$. As a result, there was no change in the colour of the solution (Figure S6a), proving that MB cannot be decreased in the presence of NaBH_4 . However, when different amounts of the NBP-PC-Zn catalyst (0.2 and 0.4 mg) were added to the reaction mixture individually, MB reduction started but was not fully completed (Figure S6b,c). For 0.2 and 0.4 mg, the calculated k_{app} values are 0.0908 and 0.1558 min^{-1} , respectively. According to Figure S6d's plot of $\ln(A_t/A_0)$ vs. time, this is due to a lack of catalytic sites or there are no sufficient electron clouds to speed up the reduction in the MB dye.

2.13. Mechanism of Dye Reduction

Figure S7a shows the structural modifications of MB, CV, and NB to their corresponding reduced forms of LMB, RCV, and RNB over metal-free catalysts. The interaction of the reducing agent and organic dyes in this metal-free catalytic reduction system took place on the regions of the surface of the rich electron cloud. On the other hand, the reaction pathways of MB, CV, and NB reduction by metal-free catalysts, in particular N, B, and P-doped carbon materials, have been described rather infrequently. Here, we suggested a method for reducing MB with NaBH_4 while using metal-free catalysts. Figure 5 illustrates a potential catalytic pathway for dye reduction over a catalyst. The first step involved the release of a H atom from the adsorbed BH_4 onto the NBP-PC-Zn catalyst's surface. At the same time, dyes were also adsorbed on the catalyst surfaces, activating them for a subsequent reduction [45]. The electrical effect brought on by N, B, and P-doping effects should be primarily responsible for the NBP-PC. Due to the minor lattice mismatch, the doped atoms can easily be integrated into the carbon matrix while the dopants can control the electrical structures. Finally, organic dyes were reduced as a result of catching electrons from NaBH_4 due to their electrophilic character. This implies that MB and NaBH_4 compete for adsorption on the NBP-PC-Zn surface. The reaction mechanism may be explained by the Langmuir–Hinshelwood model [94], and LMB is subsequently produced as it desorbs from the catalyst surface and enters the solution.

2.14. Effect of Catalyst Dosage and Temperature

For a better understanding of the catalytic behaviour, the reduction in MB dye mediated by the NBP-PC-Zn was further carried out under varied reaction conditions. Figure S7a displays the k_{app} value for the reduction in MB over catalysts with various dosages. As

seen, the k_{app} value increases quickly when the catalyst dosage is raised from 0.2 to 1.4 mg, then decreases somewhat when the dosage is raised to 1.0 mg. With the strongest catalytic activity, the 1.0 mg of catalyst had the maximum reduction rate of 0.2473 min^{-1} across the doses at 25°C . Therefore, 1.0 mg of the catalyst were utilized for this study.

Regarding the reaction temperature, the catalytic performance for MB reduction was investigated for kinetic research. As shown in Figure S7b, the k_{app} value rises as the reaction temperature rises from 25 to 55°C , indicating that a higher reaction temperature is advantageous for accelerating reaction kinetics. The values of the MB reduction rate constants for the range of temperatures range from 25 to 55°C . The k_{app} values vary from 0.2473 to 0.27431 min^{-1} , respectively. The reaction activation energy (E_a) was calculated using the Arrhenius method [95]. The E_a of MB reduction catalyzed by NBP-PC-Zn was calculated to be $2.880 \text{ KJ mol}^{-1}$ from the plot of $\ln(k)$ vs. $1/T$ (insert Figure S7b).

2.15. Simultaneous Reduction of Dyes

We carried out the simultaneous dye reduction experiment with each pair of MB, NB, and CV in order to more accurately mimic the genuine contaminated water sample. The reduction times for the cationic dye mixtures (MB + CV), (CV + NB), and (NB + MB) are depicted in Figure 7a–c, respectively. Notably, the same experimental conditions were used to maintain the dye concentration for each dye. Because there was a significant excess of NaBH_4 used in the reduction of these dyes, these reactions were assumed to be pseudo-first order, and the values of k_{app} were determined by plotting $\ln(A_t/A_0)$ vs. time as seen in Figure 7d.

2.16. Stability and Reusability

Additionally, the catalyst's durability and usage were investigated. Reusability is a significant factor for material developed for particular uses. The NBP-PC-Zn catalyst was used in recycling experiments, and the results are shown in Figure 8a. The catalyst's reduction efficiency dropped with each cycle, eventually reaching 95.6%. Importantly, there are no noticeable differences between the XRD pattern (Figure 8b) and FE-TEM image (Figure 8c) of the previous catalyst and those of the fresh one. These findings support the NBP-PC excellent Zn's stability in catalyzing the MB reduction reaction. Since large catalyst surface area and good catalytic site distribution (e.g., organic functional groups, heteroatom doping, etc.) are beneficial for the interactions between the reactants, porous-structured materials play a significant role in heterogeneous catalysis. Hence, numerous studies have been conducted to apply nanoporous materials as the catalyst or catalyst support for heterogeneous reactions.

2.17. Contaminated Water Treatment

In general, the contaminants found in lake and river water, such as sand particles, organic pollutants, and microbes, may interfere with PC's ability to catalyze the reduction in organic dyes. The following tests were created to show that PC still has catalytic effects in the presence of certain impurities. The decreasing effect of organic dyes was examined using the purified solution after the river water had been centrifuged to remove any big solid contaminants. Figure 9 shows that after adding NBP-PC-Zn, MB, and NaBH_4 to the lake water under the same experimental conditions, the solution was refreshed from multicolored to colourless after 15 min, indicating that the NBP-PC-Zn catalyst was active and is a good catalyst for reducing organic dyes in contaminated water. Furthermore, the reduction efficiency of the lake water experiment was 98%, indicating that the catalyst may be used to reduce organic dyes in a real-world sample environment. Ultra-centrifugation was used to re-collect the catalyst from the reacting solution, and translucent water was produced. To conclude, the NBP-PC-Zn catalyst can accelerate the reduction in organic dyes even in lake water samples. Therefore, the metal-free catalysts used in dye reductions are expected to be cost-effective because PCs are engineered primarily for wastewater treatment. Therefore, the capital and maintenance costs are less comparable to conventional treatment

technologies. Hence, the properties associated with practicality, including simple and large-scale synthesis, low cost, and high durability should be prioritized when developing metal-free catalysts for waste water treatment applications.

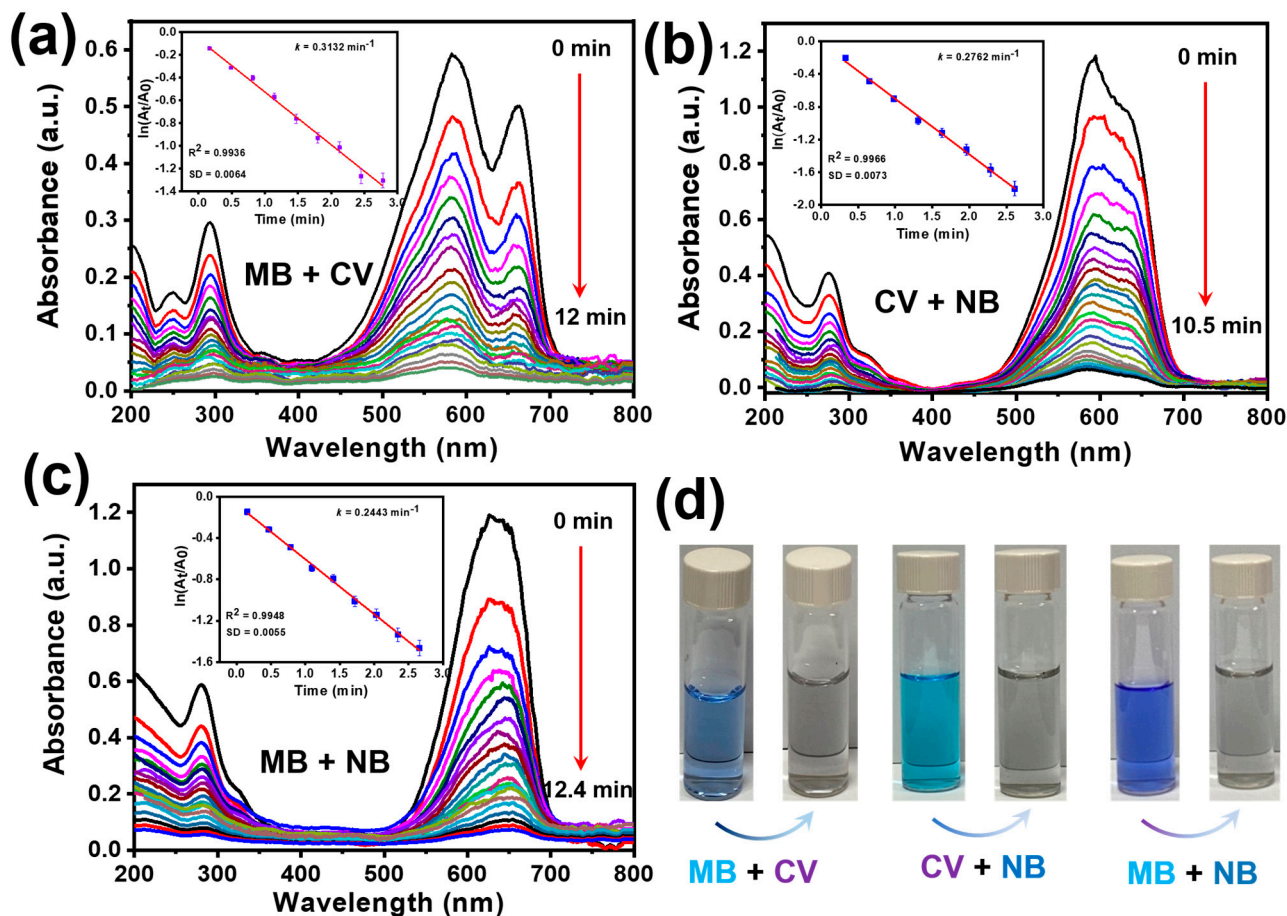


Figure 7. UV–vis spectra representing simultaneous reduction in (a) MB + CV, (b) NB + CV, (c) NB + MB dyes in the presence of the NBP-PC-Zn catalyst, (d) the photographs of colour changes after the dye reductions. Reaction conditions: solution = dyes (20 mL, 0.1 mM), NaBH_4 = 0.5 mL (0.45 mM), catalyst = 0.6 mg, 25 °C.

In recent years, metal-free catalysts have emerged as interesting candidates in the preparation of porous carbons with improved physico-chemical properties. The numerous studies on metal-free catalysts at the present time should focus on the following issues: (i) ways to develop metal-free catalysts with larger specific surface area, low cost, and ecofriendly, which can be widely used in the treatment of industrial wastewater; (ii) ways to create metal-free catalysts with enhanced efficiency and higher activity; (iii) ways to make the loaded active components (especially heteroatom doping) distribute more evenly on the surface; and (iv) ways to expand the application fields of prepare metal-free catalysts, such as the application in degradation of organic dyes in wastewater. Therefore, the strategy provided here may present alternatives for reducing organic dye content in lakes and industrial effluent. The prepared metal-free-catalyst carbons can be well dispersed in the aqueous solution due to its hydrophilic nature, and easily separated from the solution using ultracentrifugation. PC materials have many advantages including ease of preparation, large surface area, low cost, environmentally friendly nature, stability in solvents, and the presence of functional groups on their surface, which is suitable for further chemical modification.

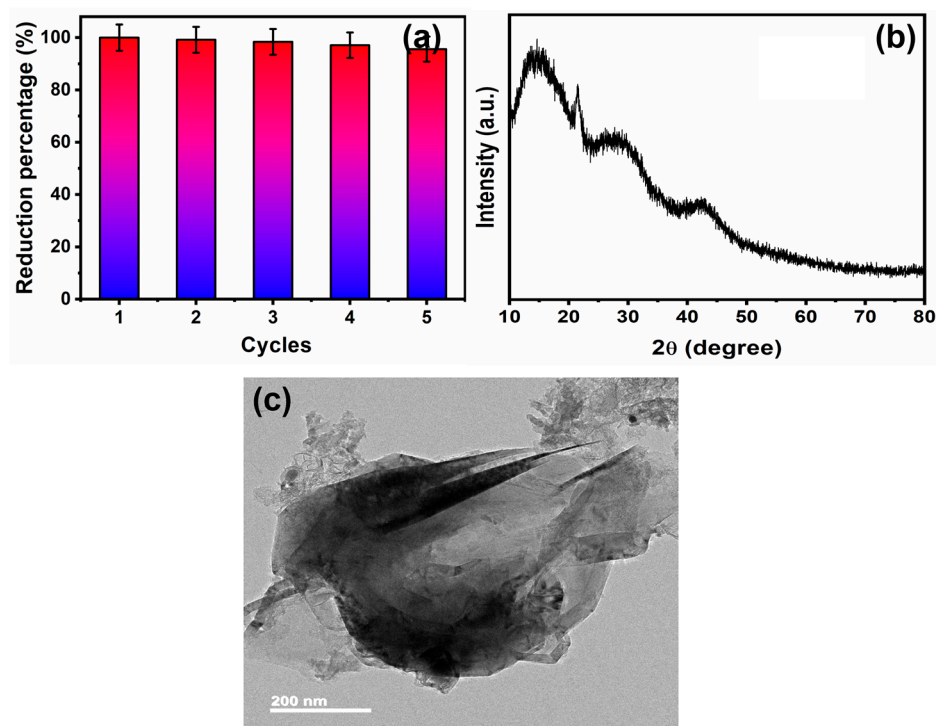


Figure 8. (a) Reusability test, (b) XRD pattern, and (c) FE-TEM image of NBP-PC-Zn after five cycles.

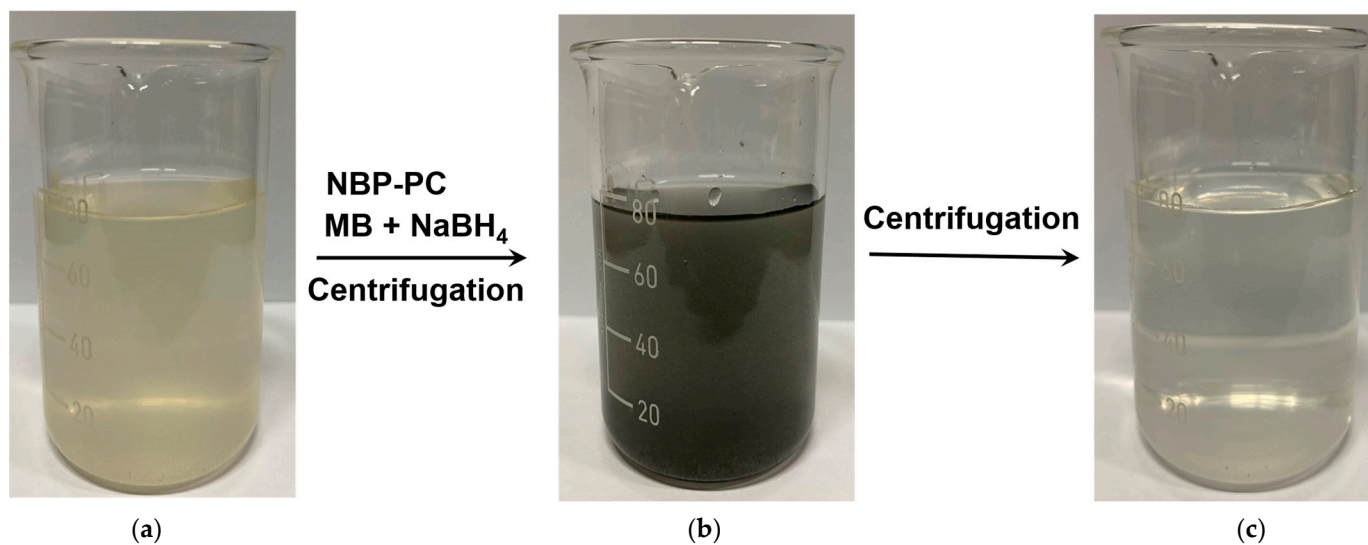


Figure 9. Photographs of dye-polluted (a) wastewater, (b) reduction after 15 min, and (c) clean water (after centrifugation).

In addition, the pore dimension, surface polarity, hydrophilicity and textural properties of PC can be functionalized through surface modification with different functional groups. This makes PC an excellent catalytic support for heterogeneous reactions. Hence, this work will not only provide a new idea for the development of metal-free catalyst with reduction catalysis, but also propose a new direction for the removal of antibiotics in real water.

3. Materials and Methods

3.1. Reagents

Magnesium(II) chloride hexahydrate ($\text{MgCl}_2 \cdot 6\text{H}_2\text{O}$, ReagentPlus®, $\geq 99.0\%$, Sigma-Aldrich-Merck, Taiwan, China), iron(III) chloride hexahydrate ($\text{FeCl}_3 \cdot 6\text{H}_2\text{O}$, ACS reagent, 97%, Sigma-Aldrich), zinc chloride (ZnCl_2 , reagent grade, $\geq 98\%$, Sigma-Aldrich), urea

(NH_2CONH_2 , ReagentPlus®, $\geq 99.5\%$, pellets), boric acid (H_3BO_3 , ACS reagent, $\geq 99.5\%$), phosphoric acid (H_3PO_4 , ACS reagent, ≥ 85 wt. % in H_2O), Nile blue chloride (NB, Sigma-Aldrich), methylene blue (MB, Acros, Taiwan, China), and crystal violet (CV, Acros, Taiwan, China) were purchased and used as received. Dragon fruit (*Hylocereus costaricensis*) peels were obtained from a local supermarket located in Taipei, Taiwan.

3.2. Material Characterization

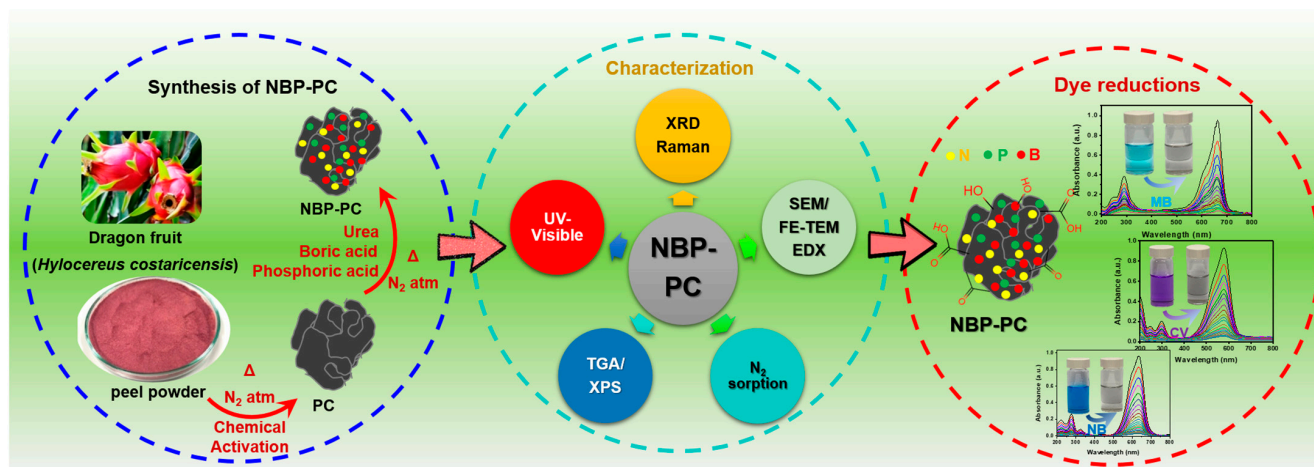
X-ray diffraction (XRD) measurements were conducted on a PANalytical (Malvern X'Pert PRO, Netherlands) diffractometer using the $\text{Cu K}\alpha$ radiation ($\lambda = 0.1541$ nm). A Fourier transform infrared spectroscopy (FTIR) spectrometer (JASCO, FT/IR-6600, CHI 1000C, Okinawa, Japan) in the range of $4000\text{--}400$ cm^{-1} was used to characterize functional groups of the sample surface, and each spectrum averaged over 32 scans. The samples were prepared as pellets using KBr (IR grade). Raman spectra were measured with an ISA Jobin Yvon T64000 spectrometer equipped with a charge coupled device (CCD) detector cooled under liquid nitrogen temperature (-196 °C). The backscattering signal was collected with a microscope using an Ar^+ laser ($\lambda = 488$ nm) as the excitation source. The sample morphology was examined by field emission transmission electron microscopy (JEOL JEM-2100F, Japan). The elemental chemical compositions of these deposited films were investigated using energy dispersive X-ray spectroscopy along with FESEM (EDS, model: AZtec, supplier: Oxford Instrument, Mumbai India). Nitrogen adsorption–desorption isotherms measured on Quantachrome Autosorb-1 at -196 °C and surface area of activated carbons was calculated by Brunauer–Emmett–Teller (BET) method. A slit pore Quenched Solid Density Functional Theory (QSDFT) equilibrium model was used to evaluate cumulative SSA, pore volume and pore size distributions. The errors in estimation of SSA (N_2) were below ± 5 m^2 g^{-1} for all tested sample. The chemical state of the elements was investigated by X-ray photoelectron spectroscopy (XPS; model: PHI 5000 Versa Prob II, supplier: ULVAC-PHI, Inc. Kanagawa, Japan). The metal ion concentration in carbon samples was determined by inductively couple plasma–optical emission spectroscopy (ICP-OES) using a PerkinElmer Optima 5300 DV instrument. The weight loss studies of the materials were performed in a NETZSCH TG-209 (Gerätebau GmbH, Selb, Germany) thermobalance under air flow (60 $\text{mL}\cdot\text{min}^{-1}$). The TGA data were obtained at a heating rate of 5 °C $\cdot\text{min}^{-1}$ and the temperature ranged from 30 to 900 °C. The UV–visible absorption spectra were carried out with a Thermo Scientific evolution 220 UV–visible spectrophotometer (Thermo Scientific, Waltham, MA, USA).

3.3. Preparation of NBP-PC-M ($M = \text{Mg}, \text{Fe}, \text{and Zn}$)

Fresh dragon fruit peels were washed in deionized water and then dried in a hot air oven for 24 h at 80 °C. After that, dried peels were ground into a fine powder. Typically, 3.0 g of powder was placed to an alumina boat crucible for the pre-carbonization process, which was carried out at 500 °C for 3 h with N_2 flow (0.9 $\text{L}\cdot\text{min}^{-1}$). Pre-carbonization resulted in the primary reactions of cross-linking, aromatization, and rearrangement of oxygen-containing groups. Chemicals and pretreated carbons were mixed in a weight ratio of $3:1$. The obtained solid was then put into a tube furnace and heated for 4 h at a rate of 5 °C min^{-1} under an atmosphere of N_2 . This process brought the solid from room temperature (RT) to 800 °C. The carbonized sample was washed with a 2.0 M HCl aqueous solution to dispose of the remaining inorganic particles after cooling to RT. The sample was then dried at 60 °C after being repeatedly rinsed with deionized water. The porous carbons were prepared, such as PC-Mg, PC-Fe, and PC-Zn, which correspond to a Mg, Fe, and Zn activation, respectively.

Typically, ~ 1.0 g of carbon sample was thoroughly mixed with 0.3 g each of urea, phosphoric acid, and boric acid before being heated at 500 °C with a mass ratio of $1:3:3$, for 3 h in a tube furnace with N_2 atmosphere. The PCs that were prepared with N, B and P co-doping were designated as NBP-PC-Mg, NBP-PC-Fe, and NBP-PC-Zn, respec-

tively. Scheme 2 illustrates the synthetic avenue involving chemical activation followed by heteroatom doping and applications.



Scheme 2. Schematic diagram illustration of the preparation (left), characterization (middle), and application (right) of NBP-PCs.

3.4. Catalytic Reduction in Dyes

The catalytic behaviour of the prepared metal-free catalysts was performed through the reduction in dyes at RT. Typically, a homogeneous mixture was created by combining 20 mL of 0.1 mM dye solution and 5 mL of 0.25 M NaBH₄. Then, 0.6 mg of carbon catalyst were added directly to the mixture under constant magnetic stirring. With a wavelength range of 200–800 nm using Thermo Scientific evolution 220 UV–visible spectrophotometer, the reaction solution's absorbance was measured. Max values for MB, CV, and NB's absorption peaks are 665, 586, and 612 nm, respectively. Table S1 lists the characteristics of dye used in this study. Additionally, different catalyst concentrations were determined under the same circumstances. Accordingly, the dyes' kinetic measurements were conducted at a set wavelength. The reaction kinetics of dye reduction over the catalyst were investigated using NaBH₄ as a hydrogen donor. The concentration of NaBH₄ was quite high and assumed to be constant throughout the process because the pseudo-first-order kinetics model was used in this work [46]. In order to determine the apparent rate constant (k_{app}), Equation (18) was applied:

$$-k_{app}t = \ln \frac{A_t}{A_0} \quad (18)$$

where A_0 and A_t were the dye concentrations at beginning and at end of the reaction period (t), respectively. The slope of the fitting line $\ln A_t/A_0$ vs. t could be used to estimate the value of k_{app} .

4. Conclusions

In summary, we have developed a simple, robust metal-free catalyst derived from dragon fruit peels using a chemical activation approach with different chemicals (MgCl₂, FeCl₃, ZnCl₂) and studied its catalytic activity. The activated carbon was further doped with heteroatoms such as N, B, P and examined for the reduction performance of organic dyes. Doping heteroatoms resulted in an increase in k_{app} values. Kinetic tests demonstrated that MB, NB, and CV dyes could be fully reduced with 0.6 mg of metal-free catalyst in 10–15 min at RT. In addition, the as-synthesized PCs materials possess abundant mesopores, large specific surface area, graphite structure, doping effects and thus excellent dye catalytic performances. Owing to the synergistic effect between N, B, and P, the co-doped catalysts not only increase electrical conductivity of catalysts to improve electron transfer, but also produce more additional active sites to intensify the catalytic performance for the reduction

in organic dyes. Based on this research, NBP-PC-Zn has the exceptional advantages of ease of preparation, low cost, and environmentally friendly nature. It may also be used to reduce the mixed organic dyes, which makes it a viable catalyst for different forms of dirty water and enables it to meet environmental cleanup requirements. We focused on NBP-PC-Zn stability and toughness so that the special qualities of this catalytic system might be applied in the chemical industry. Additionally, other uses for this catalytic system are being investigated.

Supplementary Materials: The following supporting information can be downloaded at: <https://www.mdpi.com/article/10.3390/catal13020449/s1>, Figure S1: (a) Pore size distributions, (b) Pore size vs cumulative pore volume, and (c) DTA curves of NBP-PC-Mg, NBP-PC-Fe, and NBP-PC-Zn samples; Figure S2: FT-IR spectrum of dry dragon fruit peels; Figure S3: (a) The FE-TEM dark image indicating the EDS line scan position and (b) the spectrum of a representative elements; Figure S4: (a) STEM image, (b–f) element mapping (N, B, P, C, and O elements), and (g) EDS results of NBP-PC-Mg sample; Figure S5: (a) STEM image, (b–f) element mapping (N, B, P, C, and O elements), and (g) EDS results of NBP-PC-Fe sample; Figure S6: (a) Absence of NBP-PC-Zn catalyst, (b) presence of 0.2 mg, (c) presence of 0.4 mg of NBP-PC-Zn catalyst, and (b) the corresponding plot of $\ln(A_t/A_0)$ vs. time; Figure S7: (a) The k_{app} for MB reduction of over different dosage of NBP-PC-Zn catalyst and (b) Kinetic curves of MB reduction expressed in the graph $\ln(A_t/A_0)$ vs. time (Insert: $\ln(k)$ vs. $1/T$; Table S1. Chemical and physical characteristics of the organic dyes; Table S2. Summary of XPS data obtained from fitting calculations for the B.E values of each component and their respective assignments.

Author Contributions: Conceptualization and designing of the projects, P.V.; synthesis and performing experiments, S.-T.H.; writing and editing, P.-Q.H.; methodology, writing and editing, P.V.; data curation, V.V.P. All authors have read and agreed to the published version of the manuscript.

Funding: The authors are grateful for the financial support (MOST-102-2113-M-002-009-MY3) from the Ministry of Science and Technology (MOST), Taiwan. The authors thank C.-Y. Chien of the Ministry of Science and Technology (National Taiwan University) for assistance in FE-TEM and EDS mapping experiments.

Data Availability Statement: The data presented in this study are available on request from the corresponding author.

Conflicts of Interest: The authors declare no conflict of interest.

References

1. Thomas, P.; Lai, C.W.; Johan, M.R.B. Recent developments in biomass-derived carbon as a potential sustainable material for supercapacitor-based energy storage and environmental applications. *J. Anal. Appl. Pyrolysis* **2019**, *140*, 54–85. [CrossRef]
2. Manasa, P.; Lei, Z.J.; Ran, F. Biomass waste derived low cost activated carbon from *Carchorus olitorius* (Jute fiber) as sustainable and novel electrode material. *J. Energy Storage* **2020**, *30*, 101494. [CrossRef]
3. Li, Z.; Huang, Y.; Chi, X.; Li, D.; Zhong, L.; Li, X.; Liu, C.; Peng, X. Biomass-based N doped carbon as metal-free catalyst for selective oxidation of *d*-xylose into *d*-xylonic acid. *Green Energy Environ.* **2022**, *7*, 1310–1317. [CrossRef]
4. Hao, M.; Dun, R.; Su, Y.; He, L.; Ning, F.; Zhou, X.; Li, W. *In situ* self-doped biomass-derived porous carbon as an excellent oxygen reduction electrocatalyst for fuel cells and metal–air batteries. *J. Mater. Chem. A* **2021**, *9*, 14331–14343. [CrossRef]
5. Gao, Z.; Zhang, Y.; Song, N.; Li, X. Biomass-derived renewable carbon materials for electrochemical energy storage. *Mater. Res. Lett.* **2017**, *5*, 69–88. [CrossRef]
6. Hoang, A.T.; Nižetić, S.; Cheng, C.K.; Luque, R.; Thomas, S.; Banh, T.L.; Pham, V.V.; Nguyen, X.P. Heavy metal removal by biomass-derived carbon nanotubes as a greener environmental remediation: A comprehensive review. *Chemosphere* **2021**, *287*, 131959. [CrossRef]
7. Manavalan, S.; Veerakumar, P.; Chen, S.-M.; Murugan, K.; Lin, K.-C. Binder-free modification of a glassy carbon electrode by using porous carbon for voltammetric determination of nitro isomers. *ACS Omega* **2019**, *4*, 8907–8918. [CrossRef]
8. Ji, T.; Chen, L.; Mu, L.; Yuan, R.; Knoblauch, M.; Bao, F.S.; Shi, Y.; Wang, H.; Zhu, J. Green processing of plant biomass into mesoporous carbon as catalyst support. *Chem. Eng. J.* **2016**, *295*, 301–308. [CrossRef]
9. Veerakumar, P.; Thanasekaran, P.; Subburaj, T.; Lin, K.-C. A metal-free carbon-based catalyst: An overview and directions for future research. *J. Carbon Res.* **2018**, *4*, 54. [CrossRef]
10. Guo, Z.; Cheng, M.; Ren, W.; Wang, Z.; Zhang, M. Treated activated carbon as a metal-free catalyst for effectively catalytic reduction of toxic hexavalent chromium. *J. Hazard. Mater.* **2022**, *430*, 128416. [CrossRef]

11. Rangraz, Y.; Heravi, M.M. Recent advances in metal-free heteroatom-doped carbon heterogenous catalysts. *RSC Adv.* **2021**, *11*, 23725–23778. [[CrossRef](#)]
12. Wang, Y.; Zhang, M.; Shen, X.; Wang, H.; Wang, H.; Xia, K.; Yin, Z.; Zhang, Y. Biomass-derived carbon materials: Controllable preparation and versatile applications. *Small* **2021**, *17*, 2008079. [[CrossRef](#)]
13. Johari, S. Johan, M.R. and Khaligh, N.G. An overview of metal-free sustainable nitrogen-based catalytic Knoevenagel condensation reaction. *Org. Biomol. Chem.* **2022**, *20*, 2164–2186. [[CrossRef](#)]
14. Feng, P.; Li, J.; Wang, H.; Xu, Z. Biomass-based activated carbon and activators: Preparation of activated carbon from corncob by chemical activation with biomass pyrolysis liquids. *ACS Omega* **2020**, *5*, 24064–24072. [[CrossRef](#)]
15. Zhu, Z.; Xu, Z. The rational design of biomass-derived carbon materials towards next-generation energy storage: A review. *Renew. Sustain. Energy Rev.* **2021**, *134*, 110308. [[CrossRef](#)]
16. Hu, Y.; Chen, D.; Wang, S.; Zhang, R.; Wang, Y.; Liu, M. Activation of peroxy monosulfate by nitrogen-doped porous carbon for efficient degradation of organic pollutants in water: Performance and mechanism. *Sep. Purif. Technol.* **2022**, *280*, 119791. [[CrossRef](#)]
17. Nazir, G.; Rehman, A.; Hussain, S.; Afzal, A.M.; Dastgeer, G.; Rehman, M.A.; Akhter, Z.; Al-Muhimeed, T.I.; AlObaid, A.A. Heteroatom-doped hierarchical porous carbons: Multifunctional materials for effective methylene blue removal and cryogenic hydrogen storage. *Colloids Surf. A Physicochem. Eng. Asp.* **2021**, *630*, 127554. [[CrossRef](#)]
18. Shahzad, W.; Badawi, A.K.; Rehan, Z.A.; Khan, A.M.; Khan, R.A.; Shah, F.; Ali, S.; Ismail, B. Enhanced visible light photocatalytic performance of Sr_{0.3}(Ba, Mn)_{0.7}ZrO₃ perovskites anchored on graphene oxide. *Ceram. Int.* **2022**, *48*, 24979–24988. [[CrossRef](#)]
19. Jawad, A.H.; Saud Abdulhameed, A.; Wilson, L.D.; Syed-Hassan, S.S.A.; AlOthman, Z.A.; Rizwan Khan, M. High surface area and mesoporous activated carbon from KOH-activated dragon fruit peels for methylene blue dye adsorption: Optimization and mechanism study. *Chin. J. Chem. Eng.* **2021**, *32*, 281–290. [[CrossRef](#)]
20. Arampatzidou, A.C.; Deliyanni, E.A. Comparison of activation media and pyrolysis temperature for activated carbons development by pyrolysis of potato peels for effective adsorption of endocrine disruptor bisphenol-A. *J. Colloid Interface Sci.* **2016**, *466*, 101–112. [[CrossRef](#)]
21. Chaemsanit, S.; Matan, N.; Matan, N. Effect of peppermint oil on the shelf-life of dragon fruit during storage. *Food Control* **2018**, *90*, 172–179. [[CrossRef](#)]
22. Nandiyanto, A.B.D.; Maryanti, R.; Fiandini, M.; Ragadhita, R.; Usdiyana, D.; Anggraeni, S.; Arwa, W.R.; Sh. A.; Al-Obaidi, M. Synthesis of carbon microparticles from red dragon fruit (*Hylocereus undatus*) peel waste and their adsorption isotherm characteristics. *Molekul* **2020**, *15*, 199–209. [[CrossRef](#)]
23. Gandla, D.; Wu, X.; Zhang, F.; Wu, C.; Tan, D.Q. High-performance and high-voltage supercapacitors based on N-doped mesoporous activated carbon derived from dragon fruit peels. *ACS Omega* **2021**, *6*, 7615–7625. [[CrossRef](#)] [[PubMed](#)]
24. Veerakumar, P.; Maiyalagan, T.; Raj, B.G.S.; Guruprasad, K.; Jiang, Z.; Lin, K.-C. Paper flower-derived porous carbons with high capacitance by chemical and physical activation for sustainable applications. *Arab. J. Chem.* **2020**, *13*, 2995–3007. [[CrossRef](#)]
25. Rufford, T.E.; Hulicova-Jurcakova, D.; Zhu, Z.; Lu, G.Q. A comparative study of chemical treatment by FeCl₃, MgCl₂, and ZnCl₂ on microstructure, surface chemistry, and double-layer capacitance of carbons from waste biomass. *J. Mater. Res.* **2010**, *25*, 1451–1459. [[CrossRef](#)]
26. Bedia, J.; Peñas-Garzón, M.; Gómez-Avilés, A.; Rodríguez, J.J.; Belver, C. Review on activated carbons by chemical activation with FeCl₃. *C* **2020**, *6*, 21. [[CrossRef](#)]
27. Tang, F.; Wang, L.; Liu, Y.-N. Biomass-derived N-doped porous carbon: An efficient metal-free catalyst for methylation of amines with CO₂. *Green Chem.* **2019**, *21*, 6252–6257. [[CrossRef](#)]
28. Zhang, P.; Song, X.; Yu, C.; Gui, J.; Qiu, J. Biomass-derived carbon nanospheres with turbostratic structure as metal-free catalysts for selective hydrogenation of *o*-chloronitrobenzene. *ACS Sustain. Chem. Eng.* **2017**, *5*, 7481–7485. [[CrossRef](#)]
29. Liu, D.; Dai, L.; Lin, X.; Chen, J.F.; Zhang, J.; Feng, X.; Müllen, K.; Zhu, X.; Dai, S. Chemical approaches to carbon-based metal-free catalysts. *Adv. Mater.* **2019**, *31*, 1804863. [[CrossRef](#)]
30. Zhang, H.; Wang, S.; Zhang, H.; Clark, J.H.; Cao, F. A biomass-derived metal-free catalyst doped with phosphorus for highly efficient and selective oxidation of furfural into maleic acid. *Green Chem.* **2021**, *23*, 1370–1381. [[CrossRef](#)]
31. Gholipour, B.; Shojaei, S.; Rostamnia, S.; Naimi-Jamal, M.R.; Kim, D.; Kavetsky, T.; Nouruzi, N.; Jang, H.W.; Varma, R.S.; Shokouhimehr, M. Metal-free nanostructured catalysts: Sustainable driving forces for organic transformations. *Green Chem.* **2021**, *23*, 6223–6272. [[CrossRef](#)]
32. Liu, S.; Cui, L.; Peng, Z.; Wang, J.; Hu, Y.; Yu, A.; Wang, H.; Peng, P.; Li, F.-F. Eco-friendly synthesis of N, S co-doped hierarchical nanocarbon as a highly efficient metal-free catalyst for the reduction of nitroarenes. *Nanoscale* **2018**, *10*, 21764–21771. [[CrossRef](#)]
33. Salahuddin, N.; Abdelwahab, M.A.; Akelah, A.; Elnagar, M. Adsorption of Congo red and crystal violet dyes onto cellulose extracted from Egyptian water hyacinth. *Nat. Hazards* **2021**, *105*, 1375–1394. [[CrossRef](#)]
34. Javed, M.; Qamar, M.A.; Iqbal, S.; Aljazzar, S.O.; Iqbal, S.; Khan, H.; Abourehab, M.A.; Elkaeed, E.B.; Alharthi, A.I.; Awwad, N.S.; et al. Synergistic influences of doping techniques and well-defined heterointerface formation to improve the photocatalytic ability of the S-ZnO/GO nanocomposite. *ChemistrySelect* **2022**, *7*, e202201913. [[CrossRef](#)]
35. Veerakumar, P.; Chen, S.-M.; Madhu, R.; Veeramani, V.; Hung, C.-T.; Liu, S.-B. Nickel nanoparticle-decorated porous carbons for highly active catalytic reduction of organic dyes and sensitive detection of Hg(II) ions. *ACS Appl. Mater. Interfaces* **2015**, *7*, 24810–24821. [[CrossRef](#)] [[PubMed](#)]

36. Sarwan, B.; Pare, B.; Acharya, A.D. Heterogeneous photocatalytic reduction of nile blue dye in aqueous BiOCl suspensions. *Appl. Surf. Sci.* **2014**, *301*, 99–106. [\[CrossRef\]](#)
37. Veerakumar, P.; Dhenadhayalan, N.; Lin, K.-C.; Liu, S.-B. Highly stable ruthenium nanoparticles on 3D mesoporous carbon: An excellent opportunity for reduction reactions. *J. Mater. Chem. A* **2015**, *3*, 23448–23457. [\[CrossRef\]](#)
38. Veerakumar, P.; Panneer Muthuselvam, I.; Thanasekaran, P.; Lin, K.-C. Low-cost palladium decorated on m-aminophenol-formaldehyde-derived porous carbon spheres for the enhanced catalytic reduction of organic dyes. *Inorg. Chem. Front.* **2018**, *5*, 354–363. [\[CrossRef\]](#)
39. Liang, Y.; Huang, G.; Zhang, Q.; Yang, Y.; Zhou, J.; Cai, J. Hierarchical porous carbons from biowaste: Hydrothermal carbonization and high-performance for rhodamine B adsorptive removal. *J. Mol. Liq.* **2021**, *330*, 115580. [\[CrossRef\]](#)
40. Qamar, M.A.; Shahid, S.; Javed, M.; Shariq, M.; Fadhali, M.M.; Madkhali, O.; Ali, S.K.; Syed, I.S.; Awaji, M.Y.; Shakir Khan, M.; et al. Accelerated decoloration of organic dyes from wastewater using ternary metal/g-C₃N₄/ZnO nanocomposites: An investigation of impact of g-C₃N₄ concentration and Ni and Mn doping. *Catalysts* **2022**, *12*, 1388. [\[CrossRef\]](#)
41. Liu, Y.; Xu, H.; Yu, H.; Yang, H.; Chen, T. Synthesis of lignin-derived nitrogen-doped carbon as a novel catalyst for 4-NP reduction evaluation. *Sci. Rep.* **2020**, *10*, 20075. [\[CrossRef\]](#) [\[PubMed\]](#)
42. Wang, Z.; Zhao, Z.; Baucom, J.; Wang, D.; Dai, L.; Chen, J.-F. Nitrogen-doped graphene foam as a metal-free catalyst for reduction reactions under a high gravity field. *Engineering* **2020**, *6*, 680–687. [\[CrossRef\]](#)
43. Wang, L.; Ye, R.; Jian, P.; Liu, J. Pumpkin-derived N-doped porous carbon for enhanced liquid-phase reduction of 2-methyl-4-nitrophenol. *J. Colloid Interface Sci.* **2022**, *606*, 1758–1766. [\[CrossRef\]](#)
44. Veerakumar, P.; Salamalai, K.; Thanasekaran, P.; Lin, K.-C. Simple preparation of porous carbon-supported ruthenium: Propitious catalytic activity in the reduction of ferrocyanate(III) and a cationic dye. *ACS Omega* **2018**, *3*, 12609–12621. [\[CrossRef\]](#) [\[PubMed\]](#)
45. Wang, J.; Zhang, Q.; Deng, M. Eco-Friendly preparation of biomass-derived porous carbon and Its electrochemical properties. *ACS Omega* **2022**, *7*, 22689–22697. [\[CrossRef\]](#) [\[PubMed\]](#)
46. Zhang, F.; Xiao, X.; Gandla, D.; Liu, Z.; Tan, D.Q.; Ein-Eli, Y. Bio-derived carbon with tailored hierarchical pore structures and ultra-high specific surface area for superior and advanced supercapacitors. *Nanomaterials* **2021**, *12*, 27. [\[CrossRef\]](#)
47. Fasakin, O.; Dangbegnon, J.K.; Momodu, D.Y.; Madito, M.J.; Oyedotun, K.O.; Eleruja, M.A.; Manyala, N. Synthesis and characterization of porous carbon derived from activated banana peels with hierarchical porosity for improved electrochemical performance. *Electrochim. Acta* **2018**, *262*, 187–196. [\[CrossRef\]](#)
48. Thommes, M.; Kaneko, K.; Neimark, A.V.; Olivier, J.P.; Rodriguez-Reinoso, F.; Rouquerol, J.; Sing, K.S.W. Physisorption of gases, with special reference to the evaluation of surface area and pore size distribution (IUPAC Technical Report). *Pure Appl. Chem.* **2015**, *87*, 1051–1069. [\[CrossRef\]](#)
49. Wei, T.; Zhang, Q.; Wei, X.; Gao, Y.; Li, H. A facile and low-cost route to heteroatom doped porous carbon derived from *Broussonetia Papyrifera* bark with excellent supercapacitance and CO₂ capture performance. *Sci. Rep.* **2016**, *6*, 22646. [\[CrossRef\]](#)
50. Boudou, J.P.; Bégin, D.; Alain, E.; Furdin, G.; Maréché, J.F.; Albiniaik, A. Effects of FeCl₃ (intercalated or not in graphite) on the pyrolysis of coal or coal tar pitch. *Fuel* **1998**, *77*, 601–606. [\[CrossRef\]](#)
51. Zubir, M.H.M.; Zaini, M.A.A. Twigs-derived activated carbons via H₃PO₄/ZnCl₂ composite activation for methylene blue and congo red dyes removal. *Sci. Rep.* **2020**, *10*, 14050. [\[CrossRef\]](#) [\[PubMed\]](#)
52. Figueiredo, J.L.; Pereira, M.F.R.; Freitas, M.M.A.; Órfão, J.J.M. Modification of the surface chemistry of activated carbons. *Carbon* **1999**, *37*, 1379–1389. [\[CrossRef\]](#)
53. Shoaib, G.M.; El-Sikaily, A.; El Nemr, A.; Mohamed, A.E.-D.A.; Hassan, A.A. Preparation and characterization of highly surface area activated carbons followed type IV from marine red alga (*Pterocladia capillacea*) by zinc chloride activation. *Biomass. Conv. Bioref.* **2022**, *12*, 2253–2265. [\[CrossRef\]](#)
54. Ahmad, M.A.; Puad, N.A.A.; Bello, O.S. Kinetic, equilibrium and thermodynamic studies of synthetic dye removal using pomegranate peel activated carbon prepared by microwave-induced KOH activation. *Water Resour. Ind.* **2014**, *6*, 18–35. [\[CrossRef\]](#)
55. Xie, X.Z.; Guan, W.; Ji, F.; Song, Z.; Zhao, Y. Production of biologically activated carbon from orange peel and landfill leachate subsequent treatment technology. *J. Chem.* **2014**, *2014*, 491912. [\[CrossRef\]](#)
56. Dhelipan, M.; Arunchander, A.; Sahu, A.K.; Kalpana, D. Activated carbon from orange peels as supercapacitor electrode and catalyst support for oxygen reduction reaction in proton exchange membrane fuel cell. *J. Saudi Chem. Soc.* **2017**, *21*, 487–494. [\[CrossRef\]](#)
57. Yu, D.; Wang, L.; Wu, M. Simultaneous removal of dye and heavy metal by banana peels derived hierarchically porous carbons. *J. Taiwan Ins. Chem. Eng.* **2018**, *93*, 543–553. [\[CrossRef\]](#)
58. Ohtsuka, Y.; Xu, C.; Kong, D.; Tsubouchi, N. Decomposition of ammonia with iron and calcium catalysts supported on coal chars. *Fuel* **2004**, *83*, 685–692. [\[CrossRef\]](#)
59. Ayiania, M.; Smith, M.; Hensley, A.J.R.; Scudiero, L.; McEwen, J.-S.; Garcia-Perez, M. Deconvoluting the XPS spectra for nitrogen-doped chars: An analysis from first principles. *Carbon* **2020**, *162*, 528–544. [\[CrossRef\]](#)
60. Sonkaya, Ö.; Ocakçı, Ş.; Toksoy, A.; Algi, M.P.; Algi, F. N-doped carbon nanomaterials as fluorescent pH and metal ion sensors for imaging. *Spectrochim. Acta A Mol. Biomol. Spectrosc.* **2023**, *292*, 122412. [\[CrossRef\]](#)
61. Yun, B.-N.; Du, H.L.; Hwang, J.-Y.; Jung, H.-G.; Sun, Y.-K. Improved electrochemical performance of boron doped carbon-coated lithium titanate as an anode material for sodium-ion batteries. *J. Mater. Chem. A* **2017**, *5*, 2802–2810. [\[CrossRef\]](#)

62. Rosas, J.M.; Ruiz-Rosas, R.; Rodríguez-Mirasol, J.; Cordero, T. Kinetic study of the oxidation resistance of phosphorus-containing activated carbons. *Carbon* **2012**, *50*, 1523–1537. [[CrossRef](#)]
63. Chen, Z.; Li, K.; Pu, L. The performance of phosphorus (P)-doped activated carbon as a catalyst in air-cathode microbial fuel cells. *Bioresour. Technol.* **2014**, *170*, 379–384. [[CrossRef](#)]
64. Kong, X.; Zhu, Y.; Lei, H.; Wang, C.; Zhao, Y.; Huo, E.; Lin, X.; Zhang, Q.; Qian, M.; Mateo, W.; et al. P-dual-doped multilayer graphene as an efficient carbocatalyst for nitroarene reduction: A mechanistic study of metal-free catalysis. *J. Catal.* **2018**, *359*, 233–241.
65. Li, Y.; Zhao, H.; Chen, S.; Bao, S.; Xing, F.; Jiang, B. Phosphorus-doped activated carbon catalyst for n-hexane dehydroaromatization reaction. *Catal. Commun.* **2021**, *156*, 106318. [[CrossRef](#)]
66. Sathiskumar, C.; Ramakrishnan, S.; Vinothkannan, M.; Rhan Kim, A.; Karthikeyan, S.; Yoo, D.J. Nitrogen-doped porous carbon derived from biomass used as trifunctional electrocatalyst toward oxygen reduction, oxygen evolution and hydrogen evolution reactions. *Nanomaterials* **2020**, *10*, 76. [[CrossRef](#)] [[PubMed](#)]
67. Zhu, M.; Lan, J.; Zhang, X.; Sui, G.; Yang, X. Porous carbon derived from *Ailanthus altissima* with unique honeycomb-like microstructure for high-performance supercapacitors. *New J. Chem.* **2017**, *41*, 4281–4285. [[CrossRef](#)]
68. Veerakumar, P.; Sangili, A.; Manavalan, S.; Thanasekaran, P.; Lin, K.-C. Research progress on porous carbon supported metal/metal oxide nanomaterials for supercapacitor electrode applications. *Ind. Eng. Chem. Res.* **2020**, *59*, 6347–6374. [[CrossRef](#)]
69. Zhong, G.; Xu, S.; Chao, J.; Fu, X.; Liao, W.; Xu, Y.; Liu, Z.; Cao, Y. Biomass-derived nitrogen-doped porous carbons activated by magnesium chloride as ultrahigh-performance supercapacitors. *Ind. Eng. Chem. Res.* **2020**, *59*, 21756–21767. [[CrossRef](#)]
70. Xu, Z.; Yuan, Z.; Zhang, D.; Chen, W.; Huang, Y.; Zhang, T.; Tian, D.; Deng, H.; Zhou, Y.; Sun, Z. Highly mesoporous activated carbon synthesized by pyrolysis of waste polyester textiles and $MgCl_2$: Physicochemical characteristics and pore-forming mechanism. *J. Clean. Prod.* **2018**, *192*, 453–461. [[CrossRef](#)]
71. Huang, Q.; Lu, G.; Wang, J.; Yu, J. Thermal decomposition mechanisms of $MgCl_2 \cdot 6H_2O$ and $MgCl_2 \cdot H_2O$. *J. Anal. Appl. Pyrol.* **2011**, *91*, 159–164. [[CrossRef](#)]
72. Xu, Z.; Sun, Z.; Zhou, Y.; Chen, W.; Zhang, T.; Huang, Y.; Zhang, D. Insights into the pyrolysis behavior and adsorption properties of activated carbon from waste cotton textiles by $FeCl_3$ -activation. *Colloids Surf. A* **2019**, *582*, 123934. [[CrossRef](#)]
73. Xu, Z.; Zhou, Y.; Sun, Z.; Zhang, D.; Huang, Y.; Gu, S.; Chen, W. Understanding reactions and pore-forming mechanisms between waste cotton woven and $FeCl_3$ during the synthesis of magnetic activated carbon. *Chemosphere* **2020**, *241*, 125120. [[CrossRef](#)]
74. Cazetta, A.L.; Pezoti, O.; Bedin, K.C.; Silva, T.L.; Paesano Junior, A.; Asefa, T.; Almeida, V.C. Magnetic activated carbon derived from biomass waste by concurrent synthesis: Efficient adsorbent for toxic dyes. *ACS Sustain. Chem. Eng.* **2016**, *4*, 1058–1068. [[CrossRef](#)]
75. Trinh, V.T.; Jeong, T.-Y.; Lee, B.-H.; Jeon, C.-H. Variation of char structure during anthracite pyrolysis catalyzed by Fe_2O_3 and its influence on char combustion reactivity. *Energy Fuels* **2009**, *23*, 4547–4552.
76. Sun, K.; Huang, Q.; Chi, Y.; Yan, J. Effect of $ZnCl_2$ -activated biochar on catalytic pyrolysis of mixed waste plastics for producing aromatic-enriched oil. *Waste Manag.* **2018**, *81*, 128–137. [[CrossRef](#)] [[PubMed](#)]
77. Li, B.; Hu, J.; Xiong, H.; Xiao, Y. Application and properties of microporous carbons activated by $ZnCl_2$: Adsorption behavior and activation mechanism. *ACS Omega* **2020**, *5*, 9398–9407. [[CrossRef](#)] [[PubMed](#)]
78. Lou, B.-S.; Veerakumar, P.; Chen, S.-M.; Veeramani, V.; Madhu, R.; Liu, S.-B. Ruthenium nanoparticles decorated curl-like porous carbons for high performance supercapacitors. *Sci. Rep.* **2016**, *6*, 19949. [[CrossRef](#)] [[PubMed](#)]
79. Chen, R.; Li, L.; Liu, Z.; Lu, M.; Wang, C.; Li, H.; Ma, W.; Wang, S. Preparation and characterization of activated carbons from tobacco stem by chemical activation. *J. Air Waste Manag. Assoc.* **2017**, *67*, 713–724. [[CrossRef](#)] [[PubMed](#)]
80. Benzigar, M.R.; Talapaneni, S.N.; Joseph, S.; Ramadass, K.; Singh, G.; Scaranto, J.; Ravon, U.; Al-Bahily, K.; Vinu, A. Recent advances in functionalized micro and mesoporous carbon materials: Synthesis and applications. *Chem. Soc. Rev.* **2018**, *47*, 2680–2721. [[CrossRef](#)]
81. Zacharska, M.; Bulusheva, L.G.; Lisitsyn, A.S.; Beloshapkin, S.; Guo, Y.; Chuvilin, A.L.; Shlyakhova, E.V.; Podyacheva, O.Y.; Leahy, J.J.; Okotrub, A.V.; et al. Factors influencing the performance of Pd/C catalysts in the green production of hydrogen from formic acid. *ChemSusChem* **2017**, *10*, 720–730. [[CrossRef](#)] [[PubMed](#)]
82. Nie, R.; Miao, M.; Du, W.; Shi, J.; Liu, Y.; Hou, Z. Selective hydrogenation of C=C bond over N-doped reduced graphene oxides supported Pd catalyst. *Appl. Catal. B* **2016**, *180*, 607–613. [[CrossRef](#)]
83. Qamar, M.A.; Javed, M.; Shahid, S. Designing and investigation of enhanced photocatalytic and antibacterial properties of 3d (Fe, Co, Ni, Mn and Cr) metal-doped zinc oxide nanoparticles. *Opt. Mater.* **2022**, *126*, 112211. [[CrossRef](#)]
84. Serp, P.; Machado, B. *Nanostructured Carbon Materials for Catalysis*; Royal Society of Chemistry: Cambridge, UK, 2015.
85. Li, R.; Zhao, J.; Han, D.; Li, X. One-step synthesis of B-doped mesoporous carbon as supports of Pd nanoparticles for liquid phase catalytic hydrodechlorination. *Catal. Commun.* **2017**, *97*, 116–119. [[CrossRef](#)]
86. Quílez-Bermejo, J.; Morallón, E.; Cazorla-Amorós, D. Metal-free heteroatom-doped carbon-based catalysts for ORR: A critical assessment about the role of heteroatoms. *Carbon* **2020**, *165*, 434–454. [[CrossRef](#)]
87. Abbas, Q.; Raza, R.; Shabbir, I.; Olabi, A.G. Heteroatom doped high porosity carbon nanomaterials as electrodes for energy storage in electrochemical capacitors: A review. *J. Sci. Adv. Mater. Devices* **2019**, *4*, 341–352. [[CrossRef](#)]

88. Sriram, B.; Baby, J.N.; Hsu, Y.-F.; Wang, S.-F.; Benadict Joseph, X.; George, M.; Veerakumar, P.; Lin, K.C. MnCo₂O₄ microflowers anchored on P doped g C₃N₄ nanosheets as an electrocatalyst for voltammetric determination of the antibiotic drug sulfadiazine. *ACS Appl. Electron. Mater.* **2021**, *3*, 3915–3926. [[CrossRef](#)]
89. Liu, X.; Dai, L. Carbon-based metal-free catalysts. *Nat. Rev. Mater.* **2016**, *1*, 16064. [[CrossRef](#)]
90. Mani, S.; Bharagava, R.N. Exposure to crystal violet, its toxic, genotoxic and carcinogenic effects on environment and its degradation and detoxification for environmental safety. *Rev. Environ. Contam. Toxicol.* **2016**, *237*, 71–104.
91. Duggan, P.J.; Johnson, A.A.; Rogers, R.L. Chemical reaction hazards associated with the use of sodium borohydride. In *Chemical Engineers Symposium Series*; Hemisphere Publishing Corporation: New York, NY, USA, 1994; Volume 134, p. 553.
92. Saka, C. Highly active and durable hydrogen release in NaBH₄ methanolysis reaction with sulphur and phosphorus-doped metal-free microalgal carbon nanoparticles. *Appl. Catal. B Environ.* **2021**, *292*, 120165. [[CrossRef](#)]
93. Martinez, V.; Henary, M. Nile red and Nile blue: Applications and syntheses of structural analogues. *Chem. Euro J.* **2016**, *22*, 13764–13782. [[CrossRef](#)] [[PubMed](#)]
94. Liu, J.; Li, J.; Ye, R.; Yan, X.; Wang, L.; Jian, P. Versatile bifunctional nitrogen-doped porous carbon derived from biomass in catalytic reduction of 4-nitrophenol and oxidation of styrene. *Chin. J. Catal.* **2020**, *41*, 1217–1229. [[CrossRef](#)]
95. Veerakumar, P.; Jeyapragasam, T.; Surabhi; Salamalai, K.; Maiyalagan, T.; Lin, K.C. Functionalized mesoporous carbon nanostructures for efficient removal of Eriochrome black-T from aqueous solution. *J. Chem. Eng. Data* **2019**, *64*, 1305–1321. [[CrossRef](#)]

Disclaimer/Publisher's Note: The statements, opinions and data contained in all publications are solely those of the individual author(s) and contributor(s) and not of MDPI and/or the editor(s). MDPI and/or the editor(s) disclaim responsibility for any injury to people or property resulting from any ideas, methods, instructions or products referred to in the content.